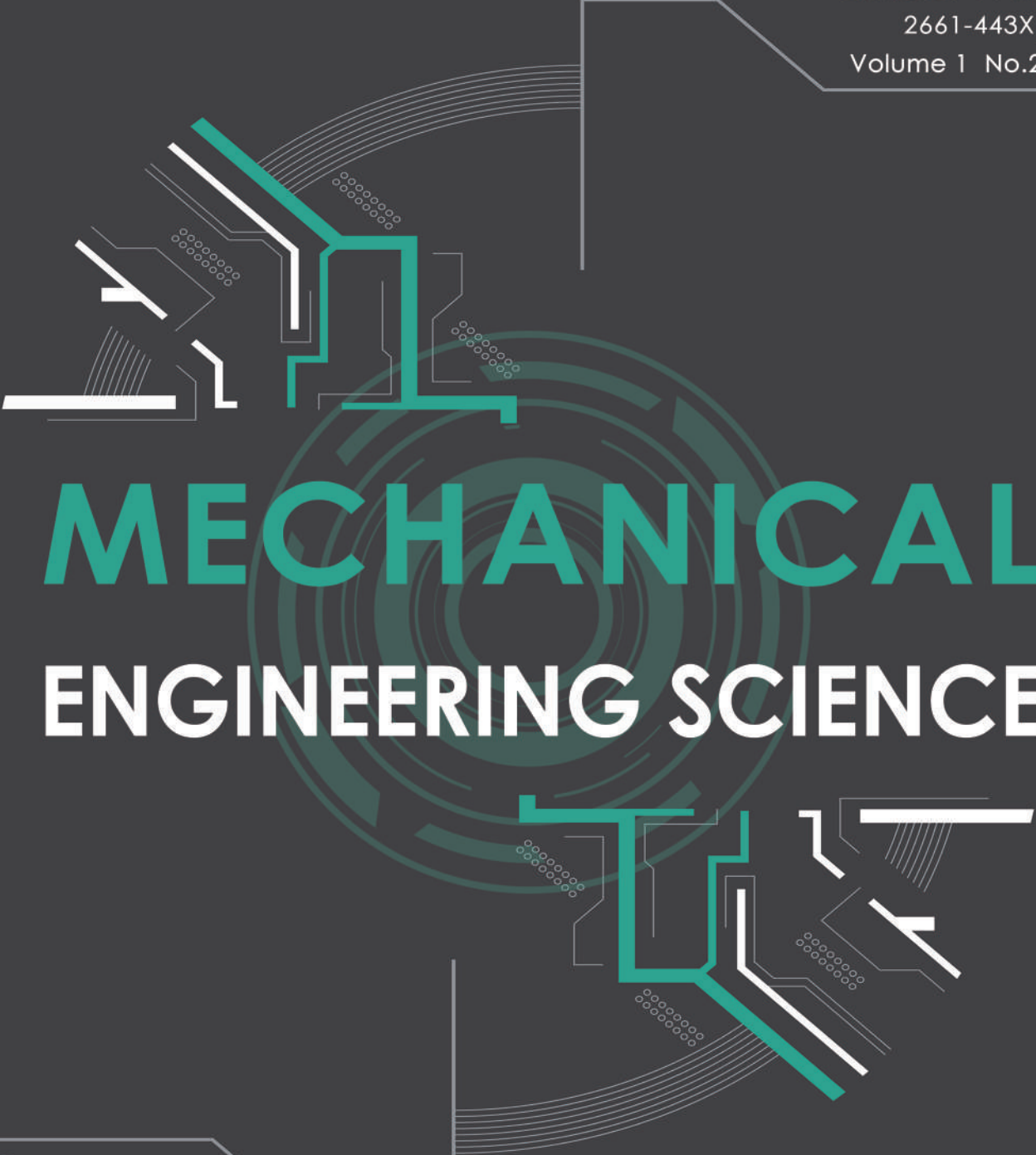


ISSN:2661-4448(online)
2661-443X(print)
Volume 1 No.2 2019



MECHANICAL ENGINEERING SCIENCE

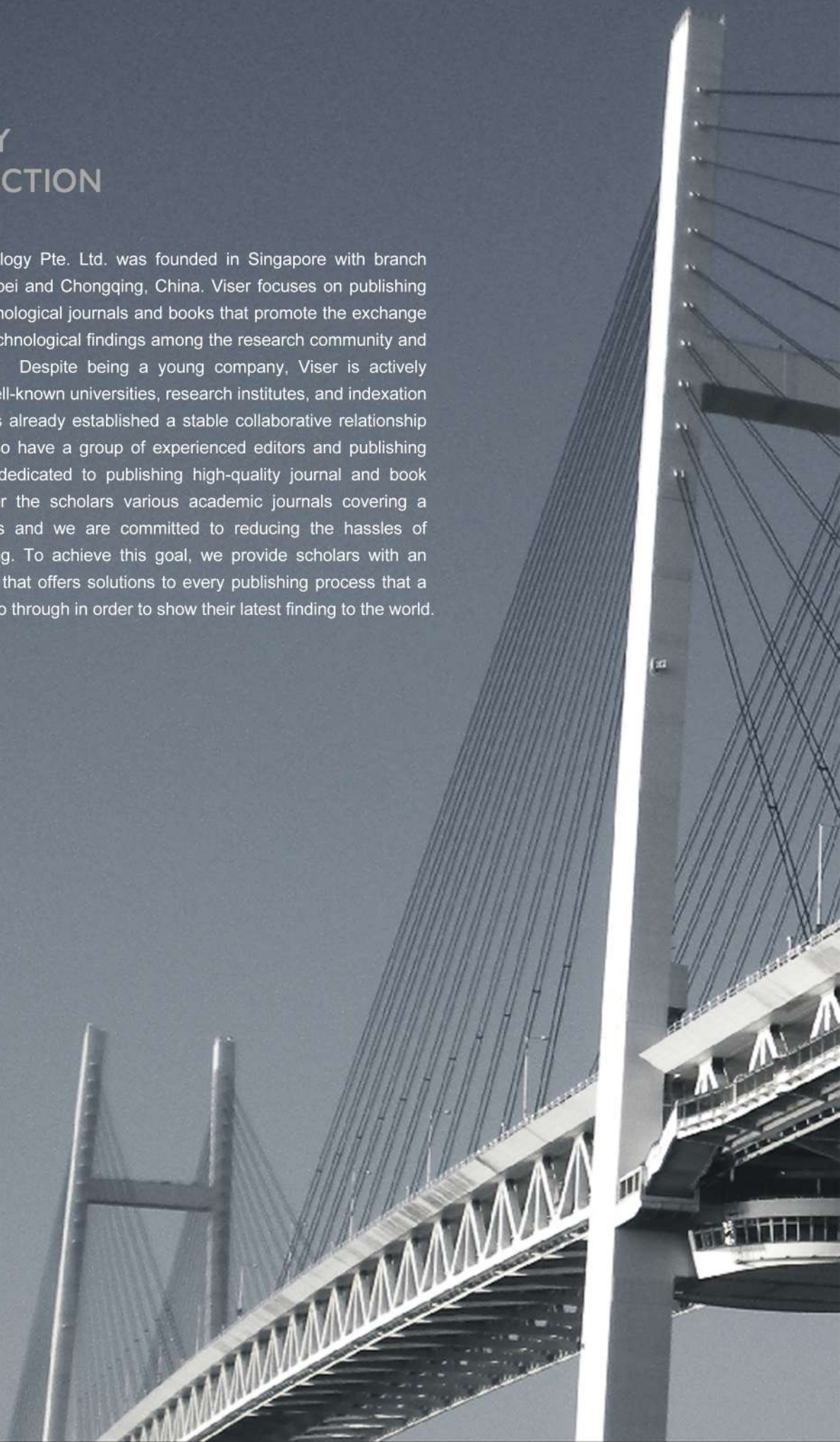


VISER

www.viserdata.com

COMPANY INTRODUCTION

Viser Technology Pte. Ltd. was founded in Singapore with branch offices in both Hebei and Chongqing, China. Viser focuses on publishing scientific and technological journals and books that promote the exchange of scientific and technological findings among the research community and around the globe. Despite being a young company, Viser is actively connecting with well-known universities, research institutes, and indexation database, and has already established a stable collaborative relationship with them. We also have a group of experienced editors and publishing experts who are dedicated to publishing high-quality journal and book contents. We offer the scholars various academic journals covering a variety of subjects and we are committed to reducing the hassles of scholarly publishing. To achieve this goal, we provide scholars with an all-in-one platform that offers solutions to every publishing process that a scholar needs to go through in order to show their latest finding to the world.



Mechanical Engineering Science

Editor-in-Chief: Kuangchao Fan

Associate Editors: Yan Shi Jianlian Cheng

Editorial Board Members:

Peitian Cong	Yuangang Wang	Gaipin Cai	Yefa Hu	Daoming Wang
Pei Feng	Yiwen Wang	Bing Chen	Xiangjie Yang	Jun Shao
Zhiqiang Xie	Yan Ran	Yang Tang	Chunsheng Song	Chunguo Zhang
Fulin Wang	Jingxiu Ling	Guorong Wang	Chunlei Yang	Linsen Shu
Renke Kang	Feng Lu	Yimin Deng	Fanglong Yin	Xiaodong Niu
Hao Zhu	Chi Ma	Youchao Sun	Xi Zhang	Lei Mao
Lei Hou	Zhanhua Song	Xiuwu Sui	Hongxia Chen	Jianbo Yu
Bo Zhou	Jianyong Li	Jianxiong Ye	Zhuanzhe Zhao	Haidong Shao
Yaobao Yin	Qiang Wang	Qinjian Zhang	Yanpu Yang	Xingang Wang
Huajie Hong	Weidong Yang	Daoyun Chen	Qiao Hu	Jinliang Xu
Dongxiao Hou	Xibing Li	Tao Wang	Jin Zhang	Zhanlong Li
Junhai Ma	Wenxin Fan	Haifeng Lyu	Zhentaο Zhang	Yuanming Huo



Publisher: Viser Technology Pte. Ltd.

ISSN: 2661-4448 (online)

2661-443X (print)

Frequency: Semi-annual

Add.: 21 Woodlands Close, #08-18,

Primz Bizhub SINGAPORE (737854)

https://www.viserdata.com/

Editors:

Yajun Lian

Yanli Liu

John Wilson

Nike Yough

Mart Chen

Qiuyue Su

Debra Hamilton

Xin Di

Jennifer M Dohy

Xiuli Li

Edward Adam Davis

Liangjun Qiu

Designer: Anson Chee

CONTENTS

Application of Xgboost Feature Extraction in Fault Diagnosis of Rolling Bearing.....	1
Xingang WANG, Chao WANG	
Embedded sensor system for five-degree-of-freedom error detection on machine tools.....	8
Yubin HUANG, Kuangchao FAN, Wei SUN	
Optimization of Process Parameters of Laser Cladding 304L Alloy Powder Based on Orthogonal Experiment	18
Linsen SHU, Bo WANG, Yayin HE	
Study on the Cutting Temperature of the Textured Tool by 3D FEA Simulation	25
Siwen TANG ,Pengfei LIU , Rui WANG, Qiulin NIU, Guoqing YANG, Wenhui LIU, Qian LIU	
Effect of Microstructures and Mechanical Properties of Large Deformation High Entropy Alloy CoCrCuFeNi in Semi-solid Isothermal Heat Treatment	33
Lajie WANG, Jiao XIONG, Jun LIU, X J YANG	
Application of Millimeter 3D Automatic Paving System in Highway Engineering Construction.....	40
Yi DONG, Jie WANG, Yijia MAO, Hua LI	

Application of Xgboost Feature Extraction in Fault Diagnosis of Rolling Bearing

Xingang WANG*, Chao WANG

Research Center of Mechanical Kinetics and Reliability, Northeastern University, Qinhuangdao, China

*Corresponding Author: Xingang WANG, Research Center of Mechanical Kinetics and Reliability, Northeastern University, Qinhuangdao, 066004, China; xgwang@neuq.neu.cn

Abstract:

Due to the difficulty that excessive feature dimension in fault diagnosis of rolling bearing will lead to the decrease of classification accuracy, a fault diagnosis method based on Xgboost algorithm feature extraction is proposed. When the Xgboost algorithm classifies features, it generates an order of importance of the input features. The time domain features were extracted from the vibration signal of the rolling bearing, the time-frequency features were formed by the singular value of the modal components that were decomposed by the variational mode decomposition. Firstly, the extracted time domain and time-frequency domain features were input into the support vector machine respectively to observe the fault diagnosis accuracy. Then, Xgboost algorithm was used to rank the importance of features and got the accuracy of fault diagnosis. Finally, important features were extracted and the extracted features were input into the support vector machine to observe the fault diagnosis accuracy. The result shows that the fault diagnosis accuracy of rolling bearing is improved after important feature extraction in time domain and time-frequency domain by Xgboost.

Keywords: fault diagnosis;rolling bearing;xgboost;feature extraction;support vector machine

1. Introduction

Nowdays, the requirement of safety and reliability of mechanical products is higher and higher^[1]. The fault diagnosis research on the most widely used rolling bearing can improve the safety of mechanical operation.

Fault diagnosis of rolling bearing usually consists of feature extraction and fault identification. The commonly used feature extraction methods include time domain, frequency domain and time-frequency domain. Zhang et al. ^[2] diagnosed the fault of rolling bearing by extracting the time domain features of the vibration acceleration signal of the rolling bearing, such as kurtosis. Kurtosis is sensitive to fault classification ^[3], while some other time domain features are not sensitive to fault classification, which may lead to low accuracy of fault recognition due to too many feature dimensions. Empirical Mode Decomposition (EMD) can adaptively decompose the signal into a series of intrinsic mode functions from high frequency to low frequency. However, this method is easy to mode mixing. In 2014, Dragomiretskiy et al. ^[4] proposed a new adaptive signal processing method-Variational Modal Decomposition (VMD). The VMD

method iteratively searched the optimal solution of the Variational model to determine the frequency center and bandwidth of each intrinsic modal component, which can realize the frequency domain subdivision of signals and the effective separation of each signal component. However, the impact of penalty parameter α and decomposition number K should be considered in VMD decomposition. Envelope entropy can be used to represent the sparse characteristics of signals. After signal decomposition, if there are more noise in signal components, the envelope entropy will be smaller. The optimal combination (K, α) can be obtained by taking the minimum value of envelope entropy as the objective function ^[5]. Wang et al. ^[6] used particle swarm optimization algorithm to optimize the VMD method to obtain the optimal (K, α) combination to decompose the signal. Liu et al. ^[7] further improved it by using particle swarm optimization based on genetic variation. Extracting the features that can easily distinguish different fault types are the most important for fault diagnosis ^[8]. Swarm intelligence optimization algorithms tend to fall into the local optimal solution, and the modal components obtained by VMD method decomposition do not completely represent fault characteristics (fault

frequency is not obvious for other noise information and interference).

At present, fault recognition systems based on machine learning algorithms are widely used. Support Vector Machine (SVM) method [11] has been widely used in many fields such as fault diagnosis and pattern recognition [12]. In terms of nonlinear problems, SVM introduces penalty parameters and kernel functions to transform them into linear problems in high dimensional space, so as to achieve effective classification. Boosting decision tree is an extensive and efficient integrated learning method. As a new method of boosting decision tree, Xgboost algorithm has been widely applied in economy and medical [13], and has achieved good results.

2. Xgboost Algorithm

The Xgboost algorithm is short for eXtreme Gradient Boosting. It is a c++ implementation of the gradient boosting machine algorithm developed by Dr. Chen Tianqi of Washington University [14]. The biggest advantage of Xgboost is that it can automatically take advantage of the CPU's multiple threads to run in parallel, while also improving the algorithm to improve the accuracy. Compared with Xgboost algorithm, the traditional Gradient Boosting Decision Tree (GBDT) algorithm only uses the information of the first derivative and the residual of the first n-1 tree to train the nth tree, which is difficult to realize distribution. Xgboost performs a second order Taylor expansion of the loss function (the objective function) and adds a regular term to the loss function to optimize the overall solution, so it can be used to weigh the decline of the objective function and the complexity of the model to avoid overfitting the model.

Suppose the model has k decision trees.

$$\hat{y}_i = \sum_{k=1}^K f_k(x_i), f_k \in \Phi \quad (1)$$

The loss function (objective function) can be defined as

$$L = \sum_i l(\hat{y}_i, y_i) + \sum_k \Omega(f_k) \quad (2)$$

where $\Omega(f) = \gamma T + \frac{1}{2} \lambda \|w\|^2$, T is the number of leaves, w is the weight of leaves. And

$$\hat{y}_i^{(t)} = \hat{y}_i^{(t-1)} + f_t(x_i) \quad (3)$$

Then the loss function can be expressed as

$$L^{(t)} = \sum_{i=1}^n l(\hat{y}_i^{(t-1)}, y_i + f_t(x_i)) + \Omega(f_t) \quad (4)$$

Taylor expansion of the loss function can be written as

$$L^{(t)} \approx \sum_{i=1}^n [l(\hat{y}_i^{(t-1)}, y_i + g_i f_t(x_i) + \frac{1}{2} h_i f_t^2(x_i))] + \Omega(f_t) \quad (5)$$

$$\text{where } g_i = \partial_{\hat{y}_i^{(t-1)}} l(\hat{y}_i^{(t-1)}, y_i) \quad (6)$$

$$h_i = \partial_{\hat{y}_i^{(t-1)}}^2 l(\hat{y}_i^{(t-1)}, y_i) \quad (7)$$

Remove the constant term, and the loss function as

$$\tilde{L}^{(t)} = \sum_{i=1}^n [g_i f_t(x_i) + \frac{1}{2} h_i f_t^2(x_i)] + \Omega(f_t) \quad (8)$$

The algorithm is transformed from traversing the sample to traversing the leaf node. Let $I_j = \{i | q(x_i) = j\}$ be defined as the j-th leaf point.

$$\begin{aligned} \tilde{L}^{(t)} &= \sum_{i=1}^n [g_i f_t(x_i) + \frac{1}{2} h_i f_t^2(x_i)] + \gamma T + \frac{1}{2} \lambda \sum_{j=1}^T w_j^2 \\ &= \sum_{j=1}^T [\sum_{i \in I_j} g_i] w_j + \frac{1}{2} (\sum_{i \in I_j} h_i + \lambda) w_j^2] + \gamma T \end{aligned} \quad (9)$$

let $G_j = \sum_{i \in I_j} g_i, H_j = \sum_{i \in I_j} h_i$, take the derivative of (9) and

set it to 0 to get the minimum of the objective function.

$$w_j = \frac{G_j}{H_j + \lambda} \quad (10)$$

Substitute the optimal solution into the objective function

$$\tilde{L}^{(t)}(q) = -\frac{1}{2} \sum_{j=1}^T \frac{G_j^2}{H_j + \lambda} + \gamma T \quad (11)$$

Xgboost is a greedy algorithm. Each training will add segmentation to the existing leaf nodes. Suppose L and R are the set of left and right nodes after segmentation.

Information gain is as equation (12)

$$\text{Gain} = \frac{1}{2} \left[\frac{G_L^2}{H_L + \lambda} + \frac{G_R^2}{H_R + \lambda} - \frac{(G_L + G_R)^2}{H_L + H_R + \lambda} \right] - \gamma \quad (12)$$

As can be seen from the above formula, Xgboost uses a certain value after division to subtract a certain value before division. In order to control the growth of the tree, the algorithm adds a threshold value γ . Only when the information gain is greater than the threshold value, the algorithm allows the nodes to segment. It is also the coefficient of the leaf nodes in the regular term, so it is equivalent to pre-pruning the tree model while optimizing the loss function.

The Xgboost algorithm uses the decision tree model to classify the attributes of child nodes, and expresses the feature importance to the current classifier through the product of weight and leaf nodes. Because Xgboost uses the idea of integration (grouping multiple weak classifiers into one classifier), it adds up the importance of the same feature to multiple trees (sorted by different attributes) and gets the F score for the importance of the feature throughout the classification process.

3. Feature Extraction

3.1 Data

The vibration acceleration signal data [15] obtained by simulating different states of rolling bearings in the electrical engineering laboratory of Case Western Reserve University (CWRU) is taken as the object (the test rig picture is shown

in fig.1). It is known that SKF deep groove ball bearing model 6205-2RS JEM was selected for the experiment, fault points with fault diameters of 0.178mm were introduced by manual discharge operation. The sampling frequency of vibration signal is 12kHz, and the motor speeds are 1797r/min. In this paper, the early vibration signal data are used to research.

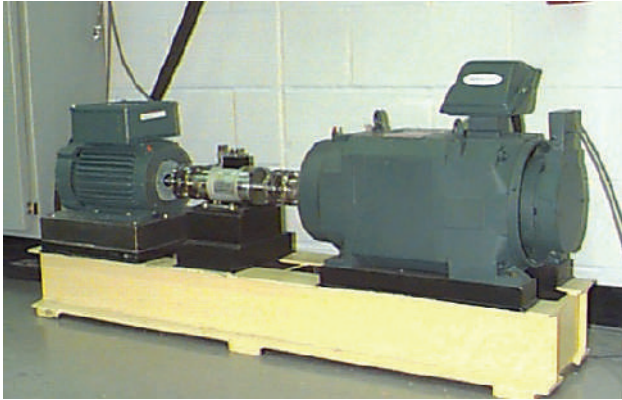


Figure 1 The test rig of CWRU. As shown in Figure 1 above, the test stand consists of a 2 hp motor (left), a torque transducer/encoder (center), a dynamometer (right), and control electronics (not shown). The test bearings support the motor shaft. Single point faults were introduced to the test bearings using electro-discharge machining with fault diameters of 7 mils, 14 mils, 21 mils, 28 mils, and 40 mils (1 mil=0.001 inches).

3.2 Data Analysis

It is assumed that the four states of the rolling bearing are healthy, bearing element fault, outer ring fault and inner ring fault, and the four states are represented by 0, 1, 2 and 3 respectively. Fig.2 to 5 are respectively the vibration signals of the bearing in four states (the data was normalized). It can be seen that the fault type of the bearing can hardly be distinguished by the time domain signals of the rolling bearing. Fig.6 shows a series of modal components and corresponding spectrum obtained by VMD ($K=6, \alpha=2000$) of no.105 data and bearing signals at the driver end of the test bench. The envelope spectrum of the first modal component was obtained as shown in fig.7. It was found that the inner ring fault frequency could be obtained, but it was not obvious. Fig.8 is the envelope spectrum obtained by enveloping the second modal component, and it can be seen that the fault characteristic frequency was obtained within the allowable error range. After enveloping all the modal components, it was found that only the second modal component had obvious fault characteristics, so it is necessary to extract the features. The failure frequency calculation formula of the inner ring ^[16] is as follows

$$f_{ir} = \frac{N}{2} \left(1 + \frac{d}{D} \cos \theta\right) f_r; \text{ Inner ring failure frequency (13)}$$

$$f_r = \frac{n}{60}; \text{ Rotational frequency (14)}$$

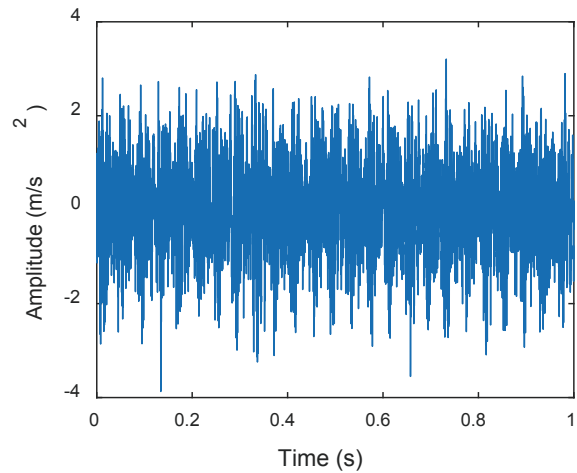


Figure 2 Healthy state vibration signal. The data of figure 2 to 8 were normalized.

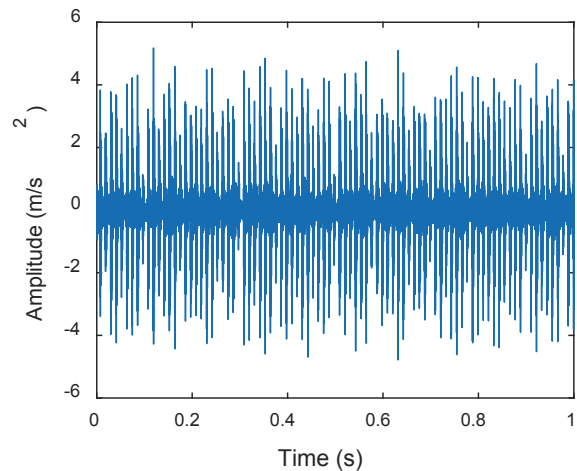


Figure 3 Outer ring fault vibration signal

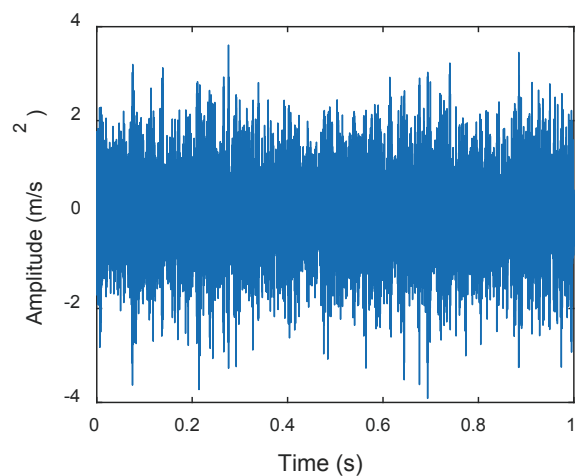


Figure 4 Bearing element fault vibration signal

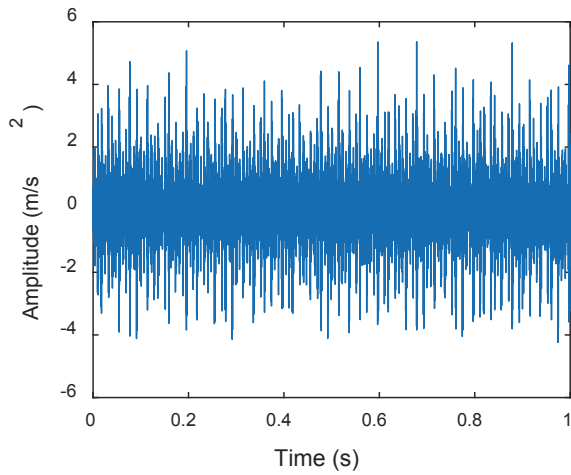


Figure 5 Inner ring fault vibration signal

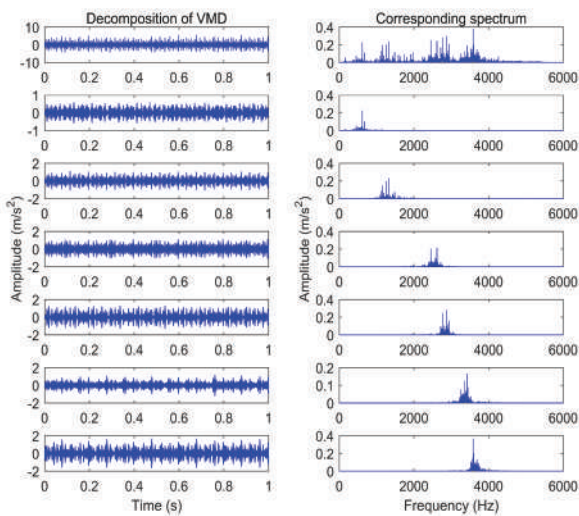


Figure 6 Modal function and spectrum of VMD. The inner ring fault signal composed of 10000 data points was decomposed into six modal components.

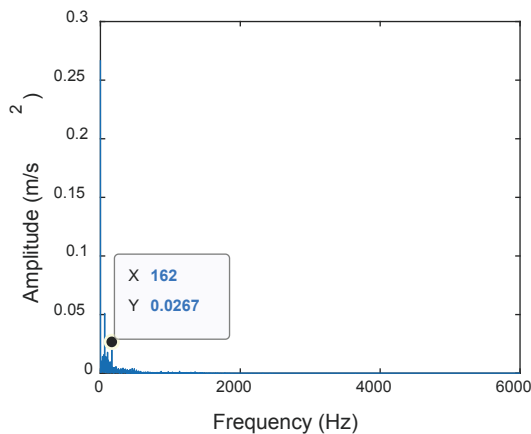


Figure 7 Envelope spectrum of the 1st modal component. Fault frequency is not obvious.

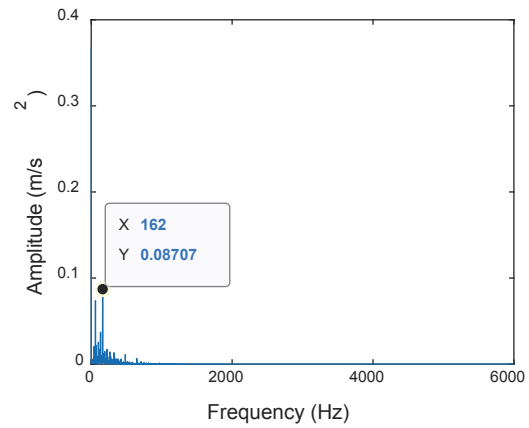


Figure 8 Envelope spectrum of the 2nd modal component. Fault frequency is obvious.

3.3 Time Domain Feature Extraction

The 10 time domain features of bearing signals were extracted: peak f_0 , peak index f_1 , skewness f_2 , kurtosis f_3 , pulse index f_4 , root mean square value f_5 , kurtosis factor f_6 , margin index f_7 , waveform index f_8 and root square amplitude f_9 , and the above features are composed into the vector $F=[f_0, f_1, \dots, f_9]$. The early bearing vibration data of CWRU were extracted, and 1024 points were taken as a group, 15 sets of time domain eigenvectors were extracted respectively from 4 kinds of load (speed) and 4 kinds of state types (in which the fault diameter is 0.178mm), and 240 sets of data were divided into 160 training sets and 80 test sets.

3.4 Time-Frequency Feature Extraction

In literature [17], the frog jump algorithm was used to optimize the variational modal decomposition by taking the minimum value of envelope entropy as the objective function. The number of modal function $K=6$ or 7 and the coefficient of quadratic penalty $\alpha=2000$ or 3000 were obtained for different fault states.

Same as 3.3, the variational mode decomposition of $K=6$ and $\alpha=2000$ was performed on the bearing data with 1024 points as a group. The six modal components obtained by decomposition of the signal are composed into the modal matrix, and the singular value decomposition (SVD) was applied to the modal matrix. 1 set of feature vectors is denoted as $F=[f_0, f_1, f_2, f_3, f_4, f_5]$, a total of 240 groups, which were divided into 160 training groups and 80 test groups.

4. Fault Identification

4.1 Fault State Recognition Based on Time Domain Feature

1) Input the obtained time domain feature vectors into the support vector machine after grid optimization for classification [18] (optimization penalty parameter c and radial basis kernel function parameter g and γ , $g, \gamma \in [2^{-15}, 2^{15}]$), and the classification accuracy was 93.125%, as shown in fig.9.

2) Input data into xgboost after parameter adjustment (learning rate =0.01, number of trees n=1000), got the accuracy of 91.25%, and got the importance order of time domain features, as shown in fig.10.

3) Take the top five features, namely peak, root mean square value, kurtosis factor, waveform index and root square amplitude were taken to form the feature vector $F'=[f_0, f_5, f_6, f_8, f_9]$ and input it into the SVM after parameter adjustment, and the accuracy was 95.625%, as shown in fig.11.

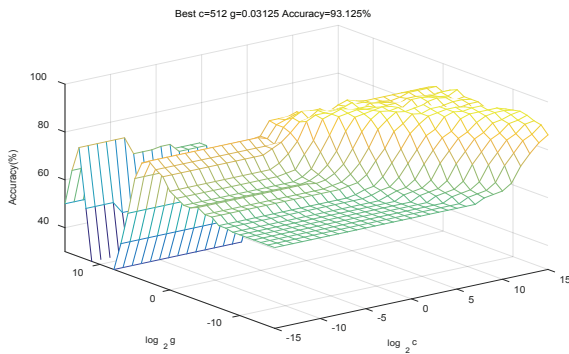


Figure 9 Time domain feature classification accuracy. In the range of c and g, grid search was carried out to get the maximum accuracy.

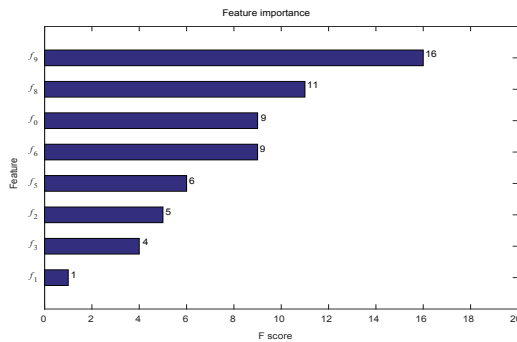


Figure 10 Order of importance of time domain features. A histogram obtained by ranking input time domain features by importance by xgboost.

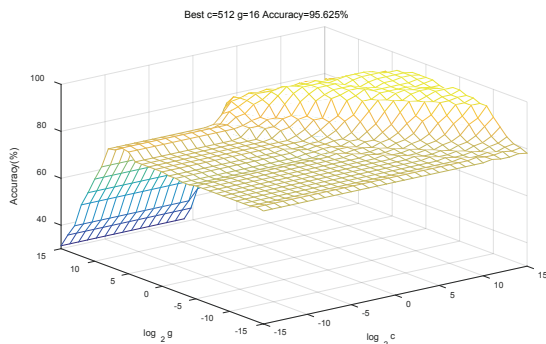


Figure 11 Classification accuracy after time domain feature extraction. After feature extraction, the accuracy obtained by grid search within the range of c and g.

4.2 Fault State Recognition Based on Time-Frequency Domain Feature

1) Input the time-frequency domain feature vectors into the support vector machine after grid optimization for classification ($c, g \in [2^{-15}, 2^{15}]$), and obtain the classification accuracy was 94.375%, as shown in fig.12.

2) Input data into Xgboost after parameter adjustment (learning rate =0.1, number of trees n=500), got the accuracy was 86.25%, and the importance order of features was obtained, as shown in fig.13.

3) Take the top five features features f_0, f_1, f_3, f_4, f_5 , and compose the vector $F'=[f_0, f_1, f_3, f_4, f_5]$, and input it into the SVM which was adjusted, and the accuracy was 95%, as shown in fig.14.

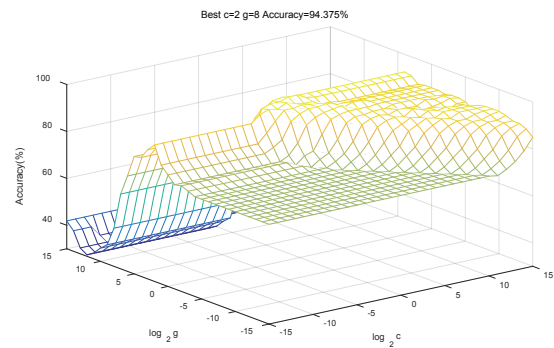


Figure 12 Time-frequency domain feature classification accuracy.

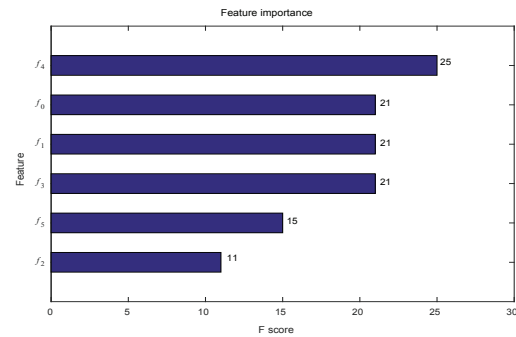


Figure 13 Order of importance of singular values

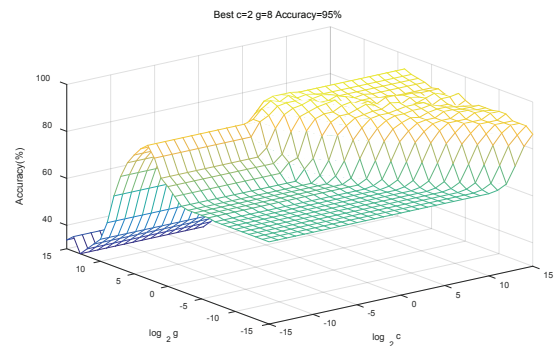


Figure 14 Classification accuracy after time-frequency domain feature extraction

4.3 Result Analysis

It can be seen from 4.2 and 4.3 that the Xgboost algorithm can improve the accuracy of fault diagnosis by ranking the time domain and time-frequency domain features respectively and extracting important features for fault diagnosis.

Doing 4 sets of experiments according to the method proposed in this article, and the results are presented in Table.1 and Table.2, it can be seen that the proposed method is more accurate than SVM and Xgboost algorithm.

Table.1. Accuracy of time domain feature extraction

Data	SVM (%)	Xgboox (%)	Xgboox+SVM (%)
1	93.125	91.5	95.625
2	83.75	75.625	85.625

Table.2. Accuracy of time-frequency domain feature extraction

Data	SVM (%)	Xgboox (%)	Xgboox+SVM (%)
1	94.375	86.25	95
2	87.5	70	88.75

5. Conclusion

In view of the influence of noise and other information on signal feature extraction in bearing fault diagnosis, Xgboost algorithm is used in this paper to order the importance of features, the important features in time domain and time frequency domain are extracted and fault diagnosis studied. Through the study, the conclusions are as follows:

1) For fault diagnosis of rolling bearing, some features directly obtained by feature extraction method do not play a role in fault diagnosis. On the contrary, as the dimension of feature vector increases, overfitting and other phenomena will occur. The results of signal analysis show that the accuracy of fault diagnosis can be improved by using Xgboost algorithm to prioritize the features of signals in time domain and time-frequency domain, and by extracting important features to reduce the feature dimension for fault diagnosis.

2)The VMD algorithm optimized by group intelligence algorithm tends to fall into the local optimal solution. The mode matrix composed by VMD is decomposed by SVD to construct the feature vector, and the important features are extracted by Xgboost algorithm, which can improve the accuracy of fault diagnosis.

Author Contributions:W.X.G. and W.C. contributed the central idea, analysed the data, and wrote the paper.

Conflict of Interest:The authors declare that there is no conflict of interest regarding the publication of this paper.

Acknowledgments:This work was supported by The National Natural Science Foundation of China (No.51475086), Fundamental Research Funds for the Central Universities of China (No. N162312001), and CAST-BISEE Foundation (No. CAST-BISEE2019-019).

References

- [1] WANG Xingang, YAN Mingming. Research on tool change time and dynamic reliability of machining process based on sensitivity analysis. *Journal of Ordnance Equipment, Engineering*, 2017, 38(1), pp.1-6. (in chinese)
- [2] ZHANG Yu, CHEN Jun, WANG Xiaofeng, et al. Application of Xgboost to fault diagnosis of rolling bearings. *Noise and Vibration Control*, 2017, 37(4), pp.166-170. (in chinese)
- [3] WANG Lei, LIU Zhiwen, MIAO Qiang, et al. Time-frequency analysis based on ensemble local mean decomposition and fast kurtogram for Rotating machinery fault diagnosis. *Mechanical Systems and Signal Processing*, 2018, 103, pp.60-75.
- [4] Dragomiretskiy K, Zosso D. Variational mode decomposition. *IEEE. Transactions on Signal Processing*, 2014, 62(3), pp.531-544.
- [5] TANG Guiji, WANG Xiaolong. Parameter optimized variational mode decomposition method with application to incipient fault diagnosis. *Journal of Xi'an Jiaotong University*. 2015, 49(5), pp.73-81. (in chinese)
- [6] WANG Xianbo, YANG Zhixin, YAN Xiaolan. Novel particle swarm optimization based variational mode decomposition method for the fault diagnosis of complex rotating machinery. *Energy*, 2018, 23(1), pp.68-79.
- [7] LIU Jianchang, QUAN He, YU Xia, et al. Rolling bearing fault diagnosis based on parameter optimization VMD and sample entropy. *Acta Automatica Sinica* (in press). (in chinese)
- [8] PAN Jun, ZI Yanyang, CHEN Jinglong, et al. Lifting Net: A novel deep learning network with layer wise feature learning from noisy mechanical data for fault classification. *IEEE. Transactions on Industrial Electronics*, 2018, 65(6), pp.4973-4982.
- [9] FU Yunxiao, JIA Limin, QIN Yong, et al. Rolling bearing fault diagnosis method based on LMD-CM-PCA. *Journal of Vibration, Measurement &Diagnosis*, 2017, 37(2), pp.249-255. (in chinese)
- [10] ZHANG Xining, ZHANG Wenwen, ZHOU Rongtong, et al. Bearing fault diagnosis method based on multiple dimensional scaling and random forest. *Journal of Xi'an Jiaotong University*, 2019, 53(8), pp.1-7. (in chinese)
- [11] Vapnik V. *The nature of statistical learning theory*, 2nd ed. Springer:New York, America; 1995; pp.163-167.
- [12] Zidi S, Moulahi T, Alaya B. Fault detection in wireless sensor networks through SVM classifier. *IEEE. Sensors Journal*, 2018, 18(1), pp.211-244.

- [13] ZHAN Chunfu, WANG Song, WU Yadong, et al. Diabetes risk prediction based on GA_Xgboost model. Computer Engineering (in press).(in chinese)
- [14] CHEN Tianqi, Guestrin C. Xgboost: A Scalable Tree Boosting System. ACM SIGKDD International Conference on Knowledge Discovery and Data Mining, ACM:California, America, 2016, pp.785-794.
- [15] Bearing Data Center Website. Available online:<http://csegroups.case.edu/bearingdatacenter/home>. (accessed on 10.5.2019)
- [16] LI Jimeng, YAO Xifeng, WANG Hui, et al. Periodic impulses extraction based on improved adaptive VMD and sparse code shrinkage denoising and its application in rotating machinery fault Diagnosis. Mechanical Systems and Signal Processing. 2019, 126, pp.568-589.
- [17] MA Hongbin, TONG Qingbin, ZHANG Yanan. Applications of optimization parameters VMD to fault diagnosis of rolling bearings. China Mechanical Engineering, 2018, 29(4), pp.390-397. (in chinese)
- [18] LIU Ruonan, YANG Boyuan, ZIO E, et al. Artificial intelligence for fault diagnosis of rotating machinery:A Review. Mechanical Systems and Signal Processing. 2018, 108, pp.33-47.

Embedded sensor system for five-degree-of-freedom error detection on machine tools

Yubin HUANG¹, Kuangchao FAN^{2*}, Wei SUN³

1 School of Mechanical Engineering, Dalian University of technology, Dalian, China

*Corresponding Author: Kuangchao FAN, No 2, Linggong road, Ganjinzi District, Dalian City, Liaoning Province, China; fan@dlut.edu.cn

Abstract:

Any linear stage of machine tool has inherent six-degree-of-freedom (6-DOF) geometric errors. Its motion control system, however, has only the position feedback. Moreover, the feedback point is not the commanded cutting point. This is the main reason why the positioning error along each axis and the volumetric error in the working space are inevitable. This paper presents a compact 5-DOF sensor system that can be embedded in each axis of motion as additional feedback sensors of the machine tool for the detection of three angular errors and two straightness errors. Using the derived volumetric error model, the feedback point can be transferred to the cutting point. The design principle of the developed 5-DOF sensor system is described. An in-depth study of systematic error compensation due to crosstalk of straightness error and angular error is analyzed. A prototype has been built into a three-axis NC milling machine. The results of a series of the comparison experiments demonstrate the feasibility of the developed sensor system.

Keywords: 5-DOF geometric motion errors; linear axis; measurement; systematic error compensation.

1. Introduction

The assessment of machine tool's volumetric errors is always an important issue in precision machining. Traditional measurement methods can only use such instruments as laser interferometer, ballbar, etc. to measure the static error of machine tool under the non-working condition^[1,2]. For the assessment of dynamic errors under cutting condition, the only method is to measure and analyze the cut specimen^[3-5]. The direct measurement method of dynamic error is rare.

It is known that the volumetric error of a 3-axis machine tool is contributed by 21 geometric errors, including 6-DOF geometric errors in each axis and three squareness errors among three axes. In order to fast measure all errors, multi-degree-of-freedom simultaneous measurement (MDFM) techniques^[6] have been developed in the past three decades. Fan developed a 3-beam 6-DOF measuring system for a linear stage^[7] and a 4-beam 6-DOF system for the XY stage^[8] based on laser Doppler displacement meters. Liu^[9] developed a 3-beam 6-DOF system based on fiber coupled laser interferometer. Feng and Cui^[10-13] et al. developed a series of 2-beam 6-DOF measurement system. Huang^[17] developed a 2-beam 5-DOF measurement system based on a monolithic prism to generate a pair of parallel laser beam.

Chen developed a 2-beam 6-DOF measurement system based on a straightness interferometer with rotational error compensation. Gillmer and Yu^[14-16] developed a single beam 6-DOF measurement system based on Polarization Optics and wavefront aberration effects.

The applications of MDFM also have received much attentions. Ni^[18,19] developed a series of 3-beam MDFM systems for monitoring errors of the coordinate measurement machine and machine tool. Chen^[20] and Li^[21] applied MDFM to simultaneously measure the 6-DOF and 5-DOF errors of a rotary axis, respectively. Commercial MDFM systems are also available on the market, such as XM-60 (Renishaw Inc, UK), XD5 (API Inc, USA) and SP1500 C5 (SIOS GmbH, Germany)^[22].

Although the above-mentioned MDFM systems are useful, however, their costs are high and they are all designed as measuring instrument for quasi-static geometric errors. The MDFM system designed for permanently fixed sensor in each linear axis of the machine tool can not only detect quasi-static errors but also dynamic geometric errors under cutting. This kind of embedded sensor system has not been seen yet.

This paper presents a low-cost and compact 5-DOF measurement system for monitoring all geometric errors except position sensing of the linear stage. A collimated

laser diode is used as the light source to reduce the system cost. The motivation of developing such an embedded sensor system is explained in section 2. The schematic of systems and the measurement principles of each error are described in section 3. In section 4, a series of experiments have been carried out to verify the feasibility of the sensor system.

2. Multi-sensor feedback NC control system

Any numerically controlled (NC) precision machine is constructed by some moving stages and a functional head. The stages can be composed of linear stages and rotary stages to form three- to multi-axis machines. The functional head characterizes the machine capability, such as the spindle head of a machine tool, the lithography head of a wafer stepper, the bonding head of an IC die bonder, the probe head of a measuring machine, etc. As it is called a precision machine, its moving position must be precisely controlled. The typical position control loop of machine tool can be seen in Fig. 1. It is noted that the commanded position is the tool point, but the feedback

position is the sensing point. If the moving stage has a tilted angle at this position, the actual position of tool (X' , functional point) is deviated from the sensing point (X) by ΔX , which is called the positioning error and is the tilted angle multiplied by the offset L . Such a positioning error is caused by the Abbe principle because the measuring axis is not in line with the functional axis [25]. In fact, each moving stage has all 6-DOF geometric errors, as shown in Fig. 2. The actual positional error in the working space is called volumetric error which is caused by related linear errors, angular errors and squareness errors induced positional errors at the functional point. Modelling the volumetric errors is dependent on the configuration of the machine tool, normally by the technique of Homogeneous Transformation Matrix (HTM) [1, 2]. Therefore, in order to compensate the volumetric error during cutting, a 5-DOF sensor system must be equipped in the machine tool and establishes a 6-DOF feedback control loop of NC machine tools, as schematically shown in Fig. 3. This is the main reason why the embedded 5-DOF sensor system is urgently needed in precision machine tools.

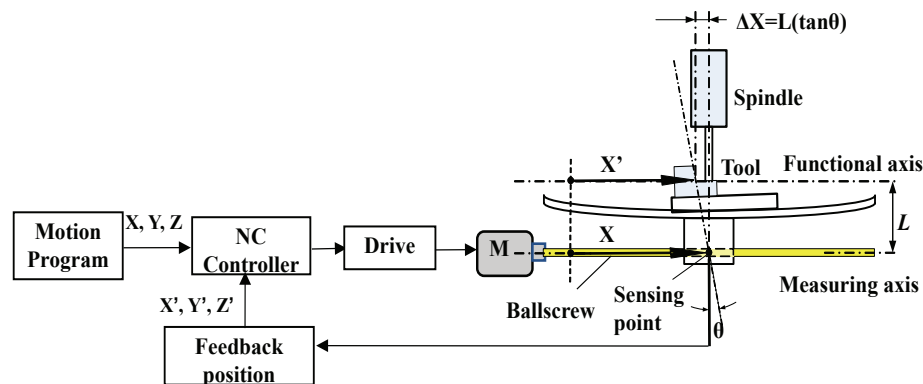


Figure 1. Typical control loop of NC machine tool

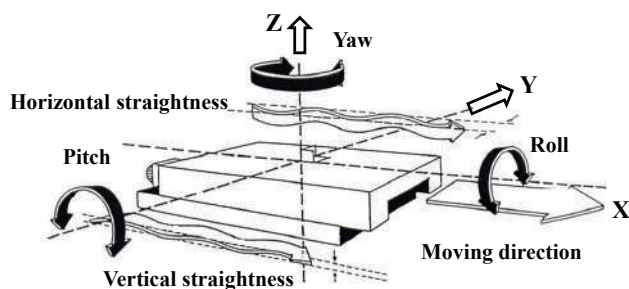


Figure 2. 6-DOF geometric errors of the linear stage

3. Design of a 5-DOF sensor system

The schematic diagram of the proposed 5-DOF sensor system is shown in Fig. 4(a). It is an extended work from our previous 4-DOF sensor system [26] with the addition of roll error sensing. The stationary part is fixed on the base of the linear stage and the moving part is moved with the motion table.

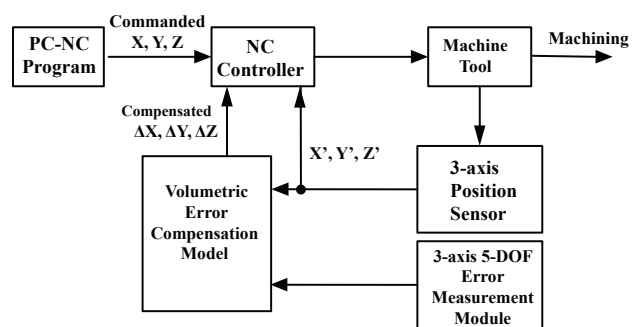


Figure 3. The proposed feedback control loop with 6-DOF sensors

In the stationary part, the laser beam from the laser diode (LD) is reflected by a mirror M1 and is then split by a polarized beam splitter (PBS) into 2 beams. The transmitted beam is used to measure straightness, yaw and pitch errors of the moving table by the quadrant photodetector (QPD3) and the autocollimator unit of focus lens (FL2) and QPD2, respectively. The reflected beam from PBS is split by a beam splitter (BS1), from which the reflected beam enters

to an autocollimator unit consisting of a focus lens (FL1) and a (QPD1) to measure the laser drift angle. The other transmitted beam turns to a outgoing beam parallel to the first beam after deflected by M2. A QPD4 detects the straightness error motion of the moving table at this point. Comparing with the vertical straightness error detected at QPD3, the difference reveals the roll error of the moving table. There are two PZT actuators embedded in the mechanism of angle steering mirror (M1) for real-time

compensation of the drifted angle of the LD. The detailed design and control of this fine-tuning mirror can be seen in our previous 4-DOF sensor system [26]. Fig. 4(b) shows the photo of the prototype of this 5-DOF sensor. When installing such a sensor system in the machine tool, the optical path is covered by a bellow shield so that the cutting chips, fluid and air disturbance can be avoided, as shown in Fig. 5. All three axes of the machine tool are treated in the same way.

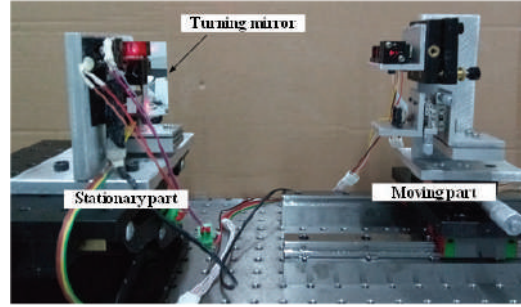
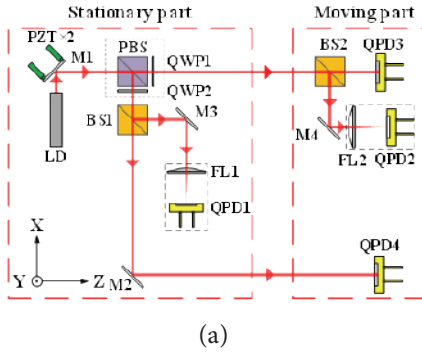


Figure 4. Schematic of the development 5-DOF measurement system: (a) optical system, (b) prototype of sensor system

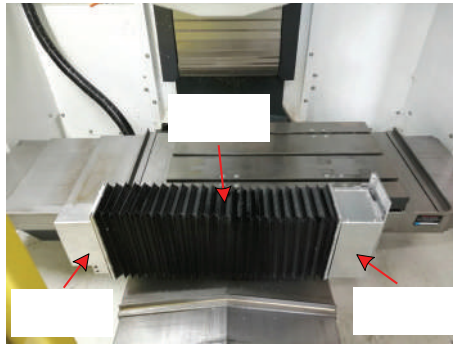


Figure 5. Mounting the 5-DOF sensor system in one axis of the machine tool

3.1. Measurement principle

It can be seen in Fig. 4(a) that the upper part of optical system is a 4-DOF sensor system [26] that detects the vertical and horizontal straightness errors, and the pitch and yaw errors, of the moving table. The center of QPD3 is defined as the point of straightness error measurement. This point is also the feedback point of measured straightness errors to the controller as illustrated in Fig. 3. Changing to different feedback point will result in different straightness error due to rigid body kinematics. Therefore, this point on the machine tool must be recorded. The corresponding straightness errors detected by the QPD3 can be expressed by:

$$\delta_x = \Delta x_{QPD3} = k_{\delta_x} \frac{(i_1 + i_4) - (i_2 + i_3)}{(i_1 + i_2 + i_3 + i_4)}$$

$$\delta_y = \Delta y_{QPD3} = k_{\delta_y} \frac{(i_1 + i_2) - (i_3 + i_4)}{(i_1 + i_2 + i_3 + i_4)} \quad (1)$$

Where, δ_x and δ_y are the straightness errors of

the measured linear stage in the X and Y directions, respectively. Δx_{QPD3} and Δy_{QPD3} are the corresponding spot movement on QPD3 respectively in the X and Y directions, i_1, i_2, i_3, i_4 indicate the output currents acquired by the QPD's 1~4 quadrants, and $k_{\delta_x}, k_{\delta_y}$ are constants obtained by the calibration experiment.

The yaw and pitch errors measured by the autocollimator unit of FL2 and QPD2 can be expressed by

$$\varepsilon_x = \frac{\Delta x_{QPD2}}{f} \quad \text{and} \quad \varepsilon_y = \frac{\Delta y_{QPD2}}{f} \quad (2)$$

where, ε_y and ε_x are yaw and Pitch errors of the measurement linear stage, respectively, Δx_{QPD2} and Δy_{QPD2} are the corresponding outputs of QPD2, and f is the focal length of FL2.

The principle of roll measurement used in this system is a typical dual parallel beam measurement method. Fig. 6 shows a simplified diagram from Fig. 4(a). The roll error of the moving stage can be obtained by the following formula:

$$\varepsilon_z = \frac{(\delta x - \delta x_4)}{L} \quad (3)$$

where, δx is the straightness error in x-direction measured by QPD3, δx_4 is the beam spot movement in x-direction measured by QPD4, L is the distance between the center of QPD3 and the center of QPD4 in the vertical direction.

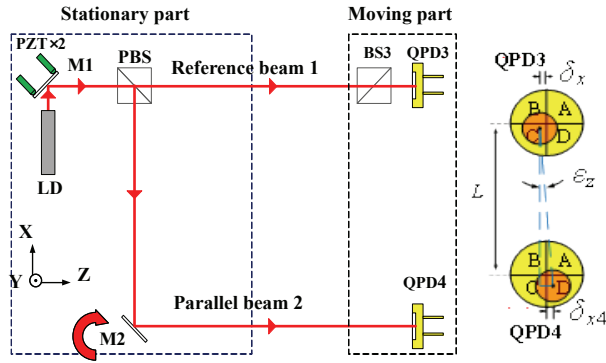


Figure 6. Measurement principle of the roll error

3.2 Feedback compensation for laser beam drift

In order to eliminate the measurement error caused by the laser beam drifts, a beam drift feedback control module proposed before [23] is integrated into the system. The angle measurement unit consisted of FL1 and QPD1 is used to measure the angular drift of the emergent laser beam. A

fine-tuning mirror driven by two PZT actuators is used as the drift feedback control mechanism to make the angle of the emerging laser beam stabilized through the PID control. To suppress the spot parallel drift caused by the change of the reflection point on the steering mirror [28], we optimized the structural design to ensure that total linear drift is within $\pm 2.56\mu\text{m}$ within the full motion of the PZTs.

4. Error compensation in angular error measurement

The measurement error compensation is a serious problem for the MDFM system, especially in the small size, highly compact measurement devices. Except the conventional crosstalk error due to the assembly error between the QPD's coordinate system and the actual coordinate system of the stage, there still have some error sources which would significantly affect the accuracy of angular error measurement.

4.1 systematic error in yaw and pitch measurement

In the proposed 5-DOF measurement system, the laser incident position of FL2 would change if the straightness error exists. As shown solid lines in Fig. 7(a), In the ideal condition, the incident position of the laser has no influence on the angular measurement since the QPD2 is set on the focus plane of FL2. In actual condition, however, due to the assembly error, the change of laser's incident position would cause a positioning shift of the focused beam spot on the QP2 surface, as shown in Fig. 7(b).

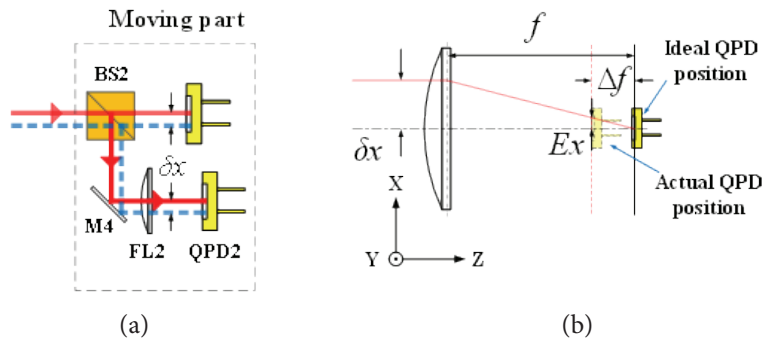


Figure 7. Systematic error of yaw and pitch angle measurement caused by the straightness error: (a) the laser's incident position shift due to the straightness error, (b) position shift of focused beam spot on the QPD surface due to the change of laser's incident position.

The relationship between the straightness error, the assembly error of QPD2's position and the position shift of the focused beam spot can be express as follows:

$$E_x = \delta x(\Delta f / f) \quad \text{and} \quad E_y = \delta y(\Delta f / f) \quad (4)$$

where, δx and δy are the straightness errors of the measured linear stage in the X and Y directions, respectively. E_x and E_y are the position shifts of the focused beam spot on the QPD2 surface, respectively. f is the focal length of FL2 and Δf is the offset distance between QPD2 surface and the focus plane of FL2 caused by assembly error. The extra shift of focused beam spot would cause a systematic measurement error E_{ex} in yaw error and E_{ey} in pitch error as

expressed by

$$E_{ex} = \frac{E_x}{f} = \delta_x \frac{\Delta f}{f^2} \quad \text{and} \quad E_{ey} = \frac{E_y}{f} = \delta_y \frac{\Delta f}{f^2} \quad (5)$$

In order to reduce the size of the 5-DOF sensor system, the focus length of FL2 is limit, which leads to a result that the measurement error caused by the change of incident position cannot be ignored. Hence, it is necessary to calibrate and compensate for these errors in the measurement software. The calibration test set-up is shown in Fig. 8(a). The incident position was measured by QPD3 of the 5-DOF system, and the autocollimator (made by

AutoMAT Co. model 5000U) was used to detect the angular error of moving stage. The calibrated results are shown in Fig. 9. It is clearly seen that the relationship between incident position change and the angular measurement error is quite linear. Due to the influence of the gap between each quadrant of QPDs, the assembly error of QPD sensing surface needs to be limited to $\pm 1.5\text{mm}$ of focal length of the FL2. When the assembly error is too large, both the autocollimator measurement principle and the defocus error compensation formula will not work properly.

In order to verify the effectiveness of error compensation, the readings of 5-DOF's measured yaw and pitch were compared to the commercial autocollimator. The comparison test is shown in Fig. 8(b) and the comparison results are shown in Fig. 10 and Fig. 11. It is seen that the residuals after compensation have been significantly reduced from about 15 arcsec to about 2 arcsec in yaw error and from about 4 arcsec to about 1.5 arcsec in pitch error. The trend of the residual curves is similar to the straightness error which will be presented in Section 5.

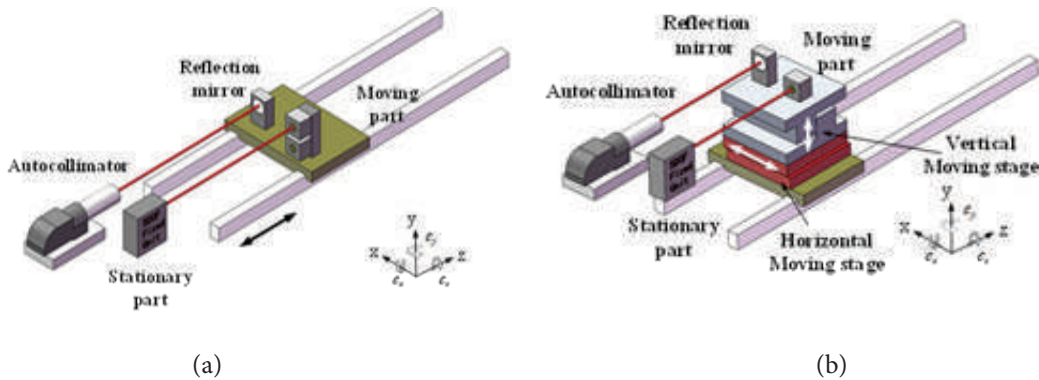


Figure 8. Experiment set-up of the yaw and pitch systematic measurement error tests. (a) Calibration set-up, (b) Comparison set-up

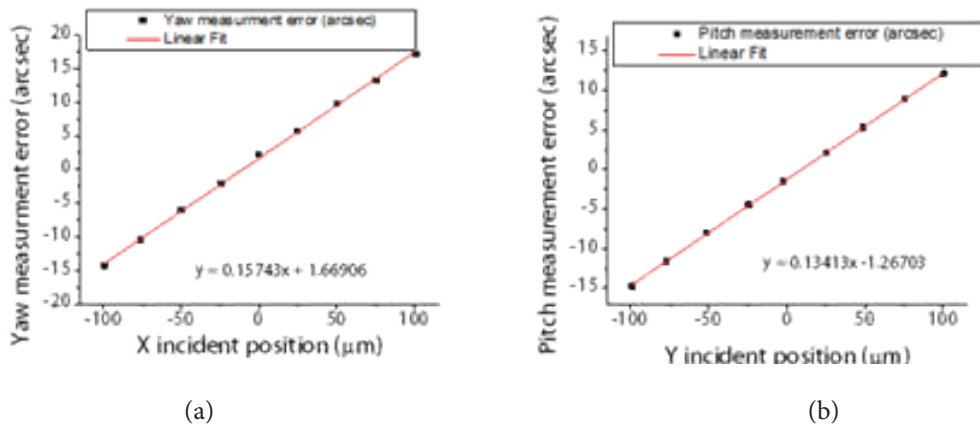


Figure 9. Calibration results of the relationship between the incident position and angular measurement error: (a) Yaw, (b) Pitch.

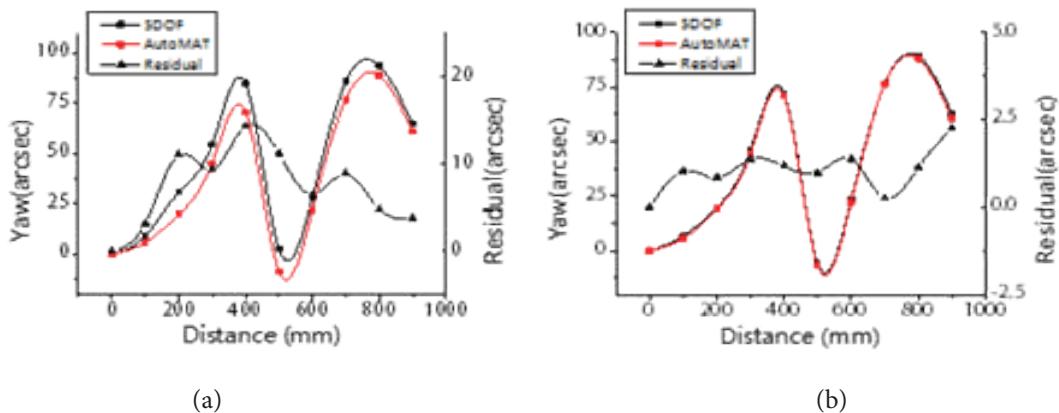


Figure 10. Systematic error of yaw angle measurement: (a) before compensation, (b) after compensation

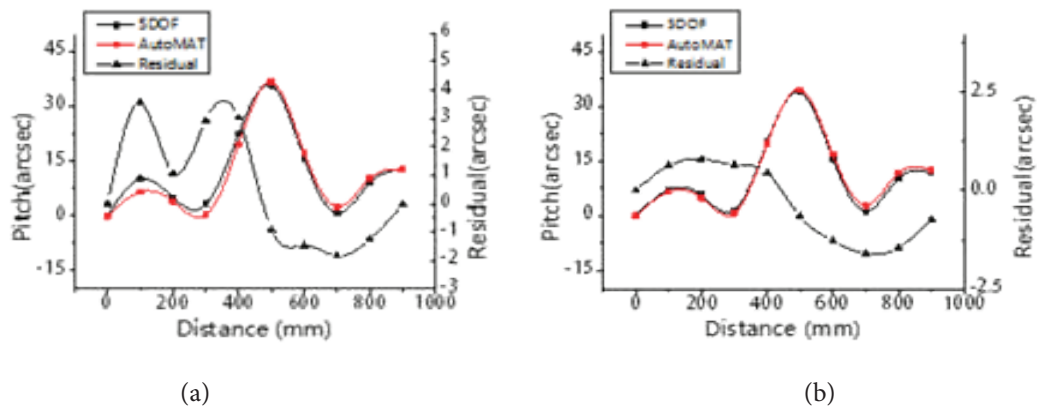


Figure 11. Systematic error of pitch angle measurement: (a) before compensation, (b) after compensation

4.2 Systematic error in roll measurement

The measurement accuracy of the principle of roll angle based on the method of dual parallel beams is significantly affected by the parallelism between the two referenced beams. If the two beams are not parallel with a small angle, a measurement error of the roll would increase with the measured distance. Therefore, an error correction model is required to separate the actual roll error from the non-parallelism induced error. This part has been comprehensively considered and solved in our previous work on the robust roll error measurement study^[27]. The technical detail is not repeated here.

5. Experiment results and discussions

5.1 Calibration experiments

The straightness errors were calibrated by a Laser Doppler

Displacement Meter (LDDM, made by Optodyne Inc. USA, model LICS-100) and the angular errors of pitch and yaw were calibrated by an autocollimator. The roll error was calibrated by an electronic level.

The calibration results of straightness measurements are shown in Fig. 12 (a) and (b). Within a measurement range of $\pm 100 \mu\text{m}$. The accuracy in each direction is within $\pm 0.5 \mu\text{m}$. The calibration results of yaw and pitch measurements are shown in Fig. 12 (c) and (d). The measurement range is $\pm 100 \text{ arcsec}$. The accuracy is within $\pm 0.5 \text{ arcsec}$ in either pitch or yaw error. The calibration result of roll measurement is shown in Fig. 12(e). The measurement range is $\pm 100 \text{ arcsec}$. The accuracy is also within $\pm 0.5 \text{ arcsec}$. These performances verify the feasibility of the developed 5-DOF sensor system.

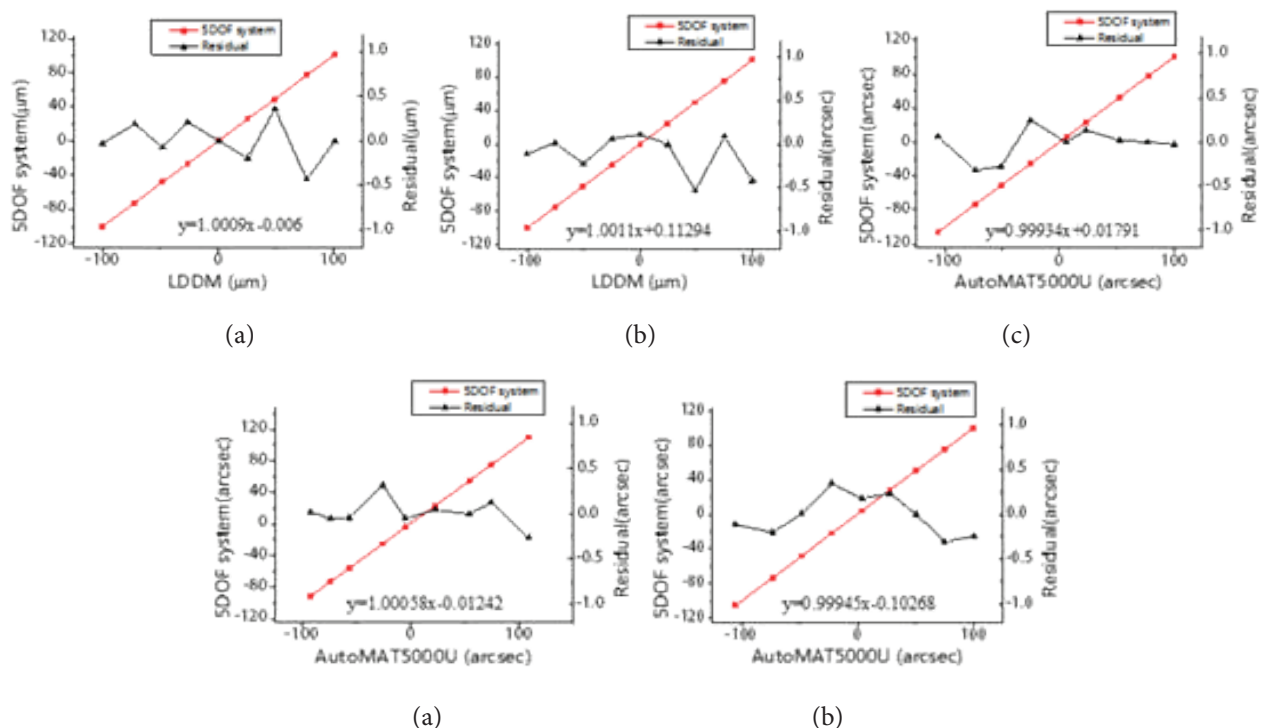


Figure 12. Results of calibration tests: (a) horizontal straightness, (b) vertical straightness, (c) yaw, (d) pitch, (e) roll.

5.2 Comparison and repeatability tests

A series of comparison experiments were made to demonstrate the effectiveness of this 5-DOF sensor system. The measurement results obtained by this sensor system are compared with the measurement results by the commercial measuring instrument. The measured distance was 900 mm with a step size of 100mm. Each comparison was repeated 5 times.

First of all the comparison experiment set-up for straightness error measurement is shown in Fig. 13(a). The straightness measurement was compared with a commercial Laser Straightness Measuring System (LSMS made by 3DFamily, Taiwan, accuracy ± 0.5 arcsec). An electronic level (made by Qianshao Co. China, model WL-2, accuracy ± 0.5 arcsec) was used to measure the roll angle in order to compensate the Bryan error in straightness

measurement. According to the Bryan principle, the straightness error measured at point A is different from that measured at point B, as shown in Fig. 13(b), and it is necessary to transform the straightness measured by the LSMS at point B to the point A for comparison. The angular induced error is corrected in association with the offset^[25] by the Bryan errors, expressed by:

$$\delta_{Ay}(z) = \delta_{By}(z) + \varepsilon_z(z)L_{BAx}(z) \quad (6a)$$

$$\delta_{Ax}(z) = \delta_{Bx}(z) - \varepsilon_z(z)L_{BAy}(z) \quad (6b)$$

The comparison results of straightness errors are given in Fig. 14(a) to (c) for the horizontal straightness and (d) to (f) for the vertical straightness of the tested linear stage. It is clearly seen that not only the trend but also the magnitude, measured errors by two systems are very coincident. The relative errors in both directions are all within $\pm 1.5 \mu\text{m}$.

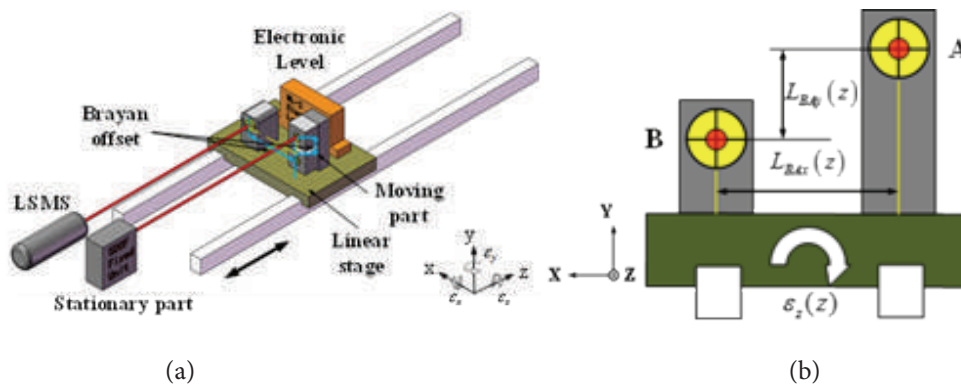


Figure 13. Comparison of straightness error measurements (a) experimental set-up, (b) Bryan error correction for different points of measurement

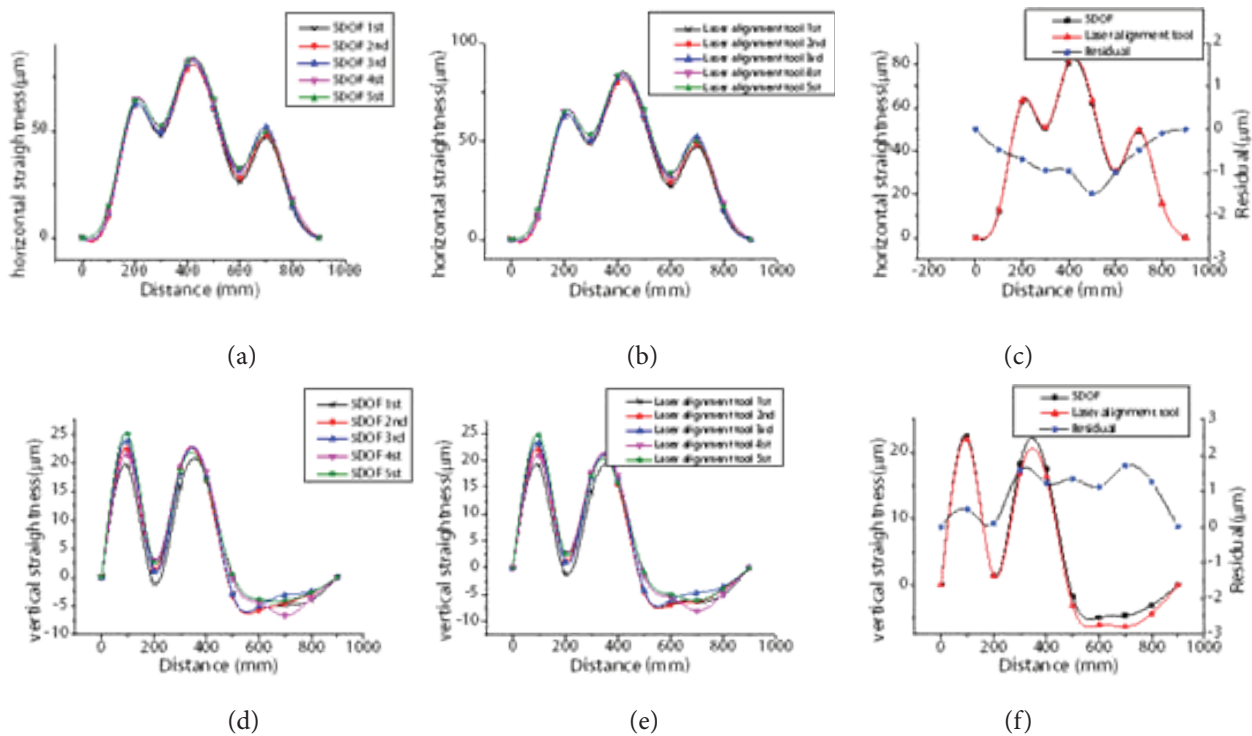


Figure 14. Straightness repeatability and comparison results: Horizontal straightness: (a) 5-DOF, (b) LSMS, (c) comparison results. Vertical straightness: (d) 5-DOF, (e) laser alignment tool, (f) comparison results.

The comparison experiment set-up for yaw and pitch error measurement has been shown in Fig. 8(b), and the comparison experiment set-up for roll error is depicted by Fig. 13(a) but without the LSMS. Fig. 15(a) to (c) show results of yaw error measurements, (d) to (f) show results of pitch error measurements, and (g) to (i) show the results

of roll error measurements. All are very satisfied. This comparison experiment can be reproduced on any eligible linear motion stage with a stroke of less than 1000mm and all 5 geometry errors are within the measurement range of the proposed 5-DOF sensing system.

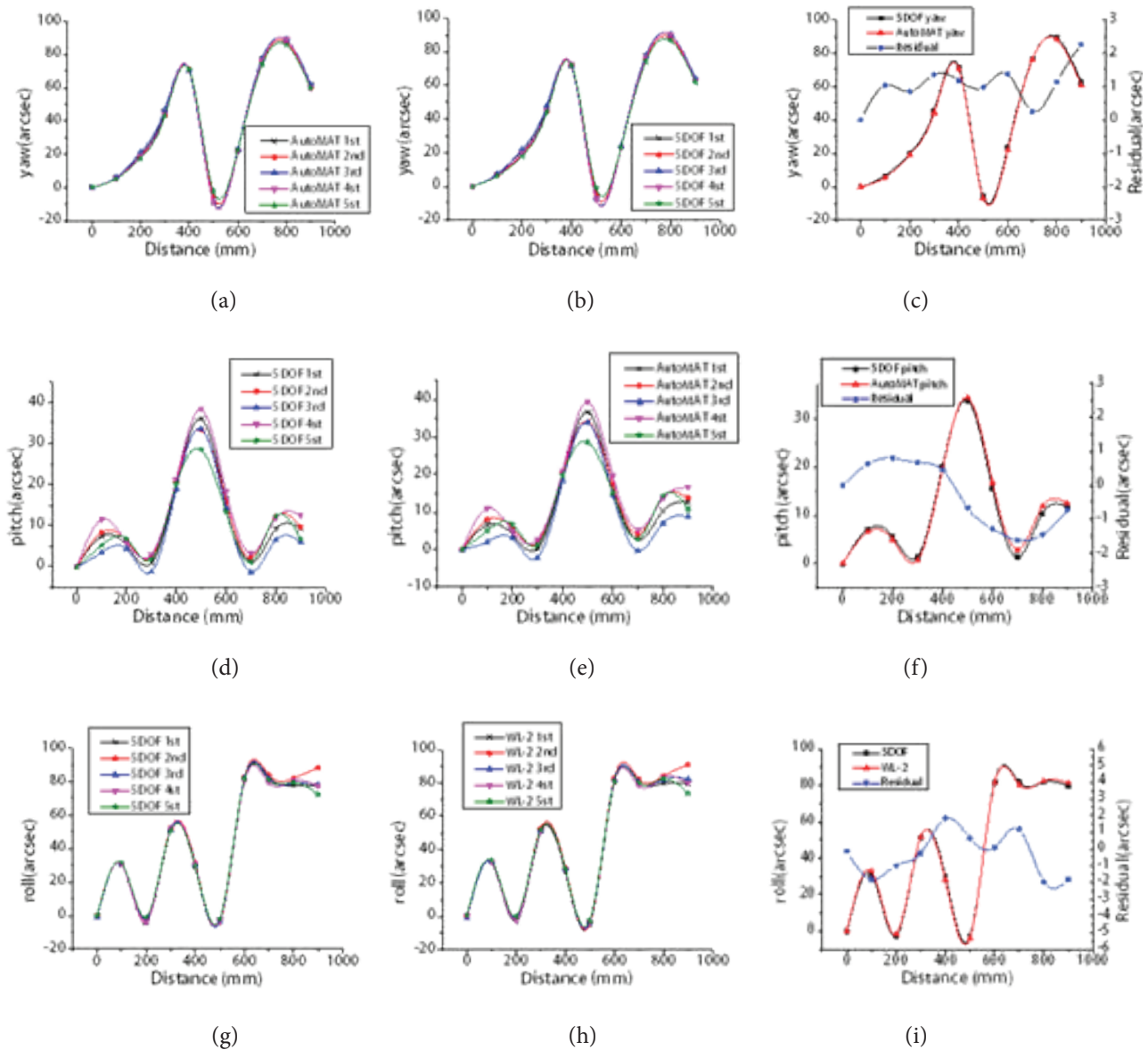


Figure 15. Angular measurement repeatability and comparison results: Yaw: (a) 5-DOF, (b) autocollimator, (c) comparison results. Pitch: (d) 5-DOF, (e) autocollimator, (f) comparison results. Roll: (g) 5-DOF, (h) electronic level, (i) comparison results.

5.3 Stability tests

The stability tests were performed under a general industrial environment without temperature control. The distance between the stationary part and moving part of the 5-DOF system remained 450 mm and the beam drift error is compensated by the feedback control in real-time. The readings of the 5-DOF system were automatically recorded at each 10 seconds and the total experiment time elapsed 5 hours.

The experimental results shown in Fig. 16 confirm the signal drift of the proposed 5-DOF system is less than 1 μm in straightness measurement, less than one arcsec in yaw and pitch measurement, and less than 2 arcsec in roll measurement, all are in 5 hours. These results prove the stability and feasibility of using this 5-DOF sensor system to detect motion errors of the linear stage of the machine tool.

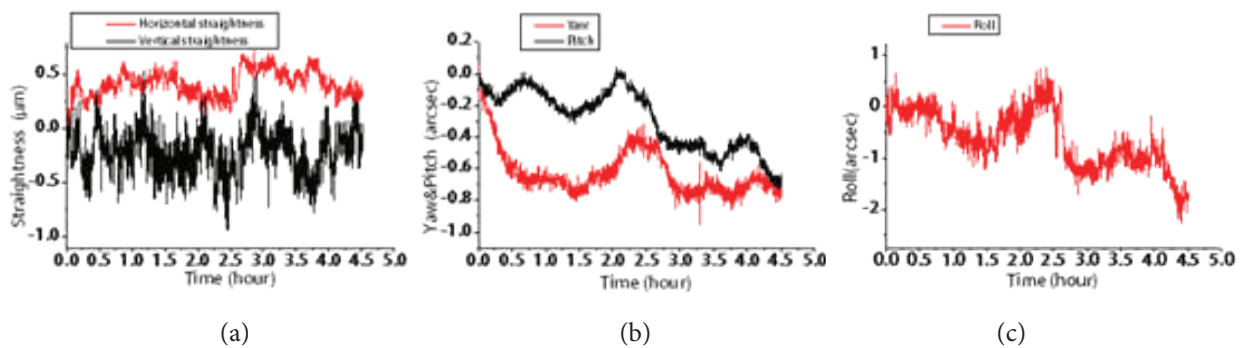


Figure 16. Results of stability experiments. (a) straightness (b) yaw&pitch (c) roll

6. Conclusions

In this paper, a 5-DOF sensor system for detecting geometric errors of each linear axis of machine tool is proposed. The system is compact in size, simple in optical configuration and low cost. It is to be installed in the machine tool as an embedded sensor to real-time detect 5-DOF geometric errors in each axis of motion. Experimental results show the feasibility and stability of the developed sensor system. It has a great potential to discover the dynamic error of the machine tool during real-cutting condition. It can also extend the current NC control loop from a single sensor feedback system to all 6 sensors feedback system so that the volumetric error compensation is possible. These are all our future works.

Author Contributions: Yubin HUANG carried out all experiments, Kuang-Chao Fan was the principal investigator of the project, and Wei Sun provided laboratory facilities.

Acknowledgement: This research was supported by the fund of The National Key Research and Development Program of China (2017YFF0204800)

References

- [1] Schwenke H, Knapp W, Haitjema H, et al. Geometric error measurement and compensation of machines—an update[J]. *CIRP Annals*, 2008, 57(2): 660-675.
- [2] Ibaraki S, Knapp W. Indirect measurement of volumetric accuracy for three-axis and five-axis machine tools: a review[J]. *International Journal of Automation Technology*, 2012, 6(2): 110-124.
- [3] Ibaraki S, Sawada M, Matsubara A, et al. Machining tests to identify kinematic errors on five-axis machine tools[J]. *Precision Engineering*, 2010, 34(3): 387-398.
- [4] Ibaraki S, Ota Y. A machining test to evaluate geometric errors of five-axis machine tools with its application to thermal deformation test[J]. *Procedia CIRP*, 2014, 14: 323-328.
- [5] Su Z, Wang L. Latest development of a new standard for the testing of five-axis machine tools using an S-shaped test piece[J]. *Proceedings of the Institution of Mechanical Engineers, Part B: Journal of Engineering Manufacture*, 2015, 229(7): 1221-1228.
- [6] Fan K C, Wang H Y, Yang H W, et al. Techniques of multi-degree-of-freedom measurement on the linear motion errors of precision machines[J]. *Advanced Optical Technologies*, 2014, 3(4): 375-386.
- [7] Fan K C, Chen M J, Huang W M. A six-degree-of-freedom measurement system for the motion accuracy of linear stages[J]. *International Journal of Machine Tools and Manufacture*, 1998, 38(3): 155-164.
- [8] Fan K C, Chen M J. A 6-degree-of-freedom measurement system for the accuracy of XY stages[J]. *Precision Engineering*, 2000, 24(1): 15-23.
- [9] Liu C H, Jywe W Y, Hsu C C, et al. Development of a laser-based high-precision six-degrees-of-freedom motion errors measuring system for linear stage[J]. *Review of scientific instruments*, 2005, 76(5): 055110.
- [10] Feng Q, Zhang B, Cui C, et al. Development of a simple system for simultaneously measuring 6DOF geometric motion errors of a linear guide[J]. *Optics express*, 2013, 21(22): 25805-25819.
- [11] Cui C, Feng Q, Zhang B, et al. System for simultaneously measuring 6DOF geometric motion errors using a polarization maintaining fiber-coupled dual-frequency laser[J]. *Optics express*, 2016, 24(6): 6735-6748.
- [12] Gao S, Zhang B, Feng Q, et al. Errors crosstalk analysis and compensation in the simultaneous measuring system for five-degree-of-freedom geometric error[J]. *Applied Optics*, 2015, 54(3): 458-466.
- [13] Zhao Y, Zhang B, Feng Q. Measurement system and model for simultaneously measuring 6DOF geometric errors[J]. *Optics express*, 2017, 25(18): 20993-21007.
- [14] Gillmer S R, Yu X, Wang C, et al. Robust high-dynamic-range optical roll sensing[J]. *Optics letters*, 2015, 40(11): 2497-2500.
- [15] Yu X, Gillmer S R, Ellis J D. Beam geometry, alignment, and wavefront aberration effects on interferometric differential wavefront sensing[J]. *Measurement Science and Technology*, 2015, 26(12): 125203..
- [16] Yu X, Gillmer S R, Woody S C, et al. Development

- of a compact, fiber-coupled, six degree-of-freedom measurement system for precision linear stage metrology[J]. *Review of Scientific Instruments*, 2016, 87(6): 065109.
- [17] Huang P, Li Y, Wei H, et al. Five-degrees-of-freedom measurement system based on a monolithic prism and phase-sensitive detection technique[J]. *Applied optics*, 2013, 52(26): 6607-6615.
- [18] Wu S M. An on-line measurement technique for machine volumetric error compensation[J]. *Ann Arbor*, 1993, 1050: 48109.
- [19] Huang P S, Ni J. On-line error compensation of coordinate measuring machines[J]. *International Journal of Machine Tools and Manufacture*, 1995, 35(5): 725-738.
- [20] Chen B, Xu B, Yan L, et al. Laser straightness interferometer system with rotational error compensation and simultaneous measurement of six degrees of freedom error parameters[J]. *Optics express*, 2015, 23(7): 9052-9073.
- [21] Li J, Feng Q, Bao C, et al. Method for simultaneous measurement of five DOF motion errors of a rotary axis using a single-mode fiber-coupled laser[J]. *Optics express*, 2018, 26(3): 2535-2545.
- [22] Mutilba U, Gomez-Acedo E, Kortaberria G, et al. Traceability of on-machine tool measurement: a review[J]. *Sensors*, 2017, 17(7): 1605.
- [23] Liu S, Zhang S, Huang Y, et al. The Method for Restraining Laser Drift Based on Controlling Mirror[J]. *Nanomanufacturing and Metrology*, 2018: 1-8.
- [24] Torng J, Wang C H, Huang Z N, et al. A novel dual-axis optoelectronic level with refraction principle[J]. *Measurement Science and Technology*, 2013, 24(3): 035902.
- [25] Bryan J B. The Abbe principle revisited: an updated interpretation[J]. *Precision Engineering*, 1979, 1(3): 129-132.
- [26] Huang Y B, Fan K C, Sun W, Liu S J. Low cost, compact 4-DOF measurement system with active compensation of beam angular drift error. *Optics Express*, 2018, 26(13): 17185-17198.
- [27] Cai Y, Yang B H, Fan K C. A robust roll angular error measurement method for precision machines. *Optics Express*, 2019, 27(6): 8027-8036.
- [28] Liu S, Tan S, Huang Y, et al. Design of a compact four degree-of-freedom active compensation system to restrain laser's angular drift and parallel drift. *Review of Scientific Instruments*, 2019, 90(11): 115002.

Optimization of Process Parameters of Laser Cladding 304L Alloy Powder Based on Orthogonal Experiment

Linsen SHU^{12*}, Bo WANG¹, Yayin HE¹

1 School of Mechanical Engineering, Shaanxi University of technology, Hanzhong, Shaanxi, China

2 Shaanxi Key Laboratory of Industrial Automation, Hanzhong, Shaanxi, China

*Corresponding Author: Linsen SHU, School of Mechanical Engineering, Shaanxi University of technology, Hanzhong, Shaanxi, 723001, China

Abstract:

In order to find the optimal combination of process parameters for laser cladding 304L alloy powder on the surface of 45 steel, a combination method of single factor test and multi-factor orthogonal experiment was used to perform the single pulse laser cladding experiment. The effects of process parameters (pulse current A, pulse width B, pulse frequency C, defocus distance D, scan velocity E) on the morphology and performance of cladding layer was studied by range analysis, and the optimal combination of cladding parameters is calculated by fuzzy comprehensive evaluation. The results show that different process parameters have different effects on the morphology of the cladding layer and scanning velocity E and defocus distance D are the most important influencing factor of cladding morphology. The effect on cladding width is $D > C > A > B > E$ and the effect on cladding height is $E > A > C > D > B$. The optimal combination of cladding width is $A_4B_4C_4D_4E_2$. The optimal combination of cladding high is $A_2B_1C_1D_4E_1$. The comprehensive optimal process parameters are pulse current 210A, pulse width 3.6ms, pulse frequency 16Hz, defocus distance +10mm and scanning speed 240mm/min. The average hardness of the cladding layer, melting pool, heat-affected zone and substrate under the optimal process parameters is 406.2 HV_{0.5}, 470.8 HV_{0.5}, 230.5HV_{0.5} and 202.0HV_{0.5}, respectively. The 304L cladding layer on 45 steel surface is stable in width, height and surface quality under comprehensive optimal parameters.

Keywords: laser optical; the optimal process; orthogonal test; 304L alloy powder; laser cladding; fuzzy comprehensive evaluation.

1. Introduction

Laser cladding is a coating technology that deposits multiple layers of composite material on the substrate to improve the physical properties of the work-piece such as wear resistance and corrosion resistance^[1-4]. Laser cladding technology is widely used in surface enhancement and wear repair of parts^[5-9]. Laser cladding technology has good adaptability and no special requirements for metal powder and substrate. It can obtain high performance alloy on cheap and low performance metal surface and can significantly improve the mechanical properties of mechanical parts^[10-11]. Steel 45 is a common material used in manufacturing machine parts. It has important industrial application value to prepare wear - resistant and corrosion - resistant cladding layer with high hardness on the surface of 45 steel.

At present, the research of preparing high performance alloy cladding layer on low performance metal has been published. Parekh R et al.^[12] studied the optimization of

cladding forming geometry and found that laser cladding process parameters had a direct impact on its geometry. Jiao X. et al.^[13] studied the influence of scanning velocity on the microstructure of cladding layer, and found that increasing velocity would induce defects. Lei J.F et al.^[14] studied the laser cladding Ni60-25% WC coating on U71Mn steel surface and obtained the optimal process parameters. Zan S.P et al.^[15] studied the laser cladding technology of 316L stainless steel powder, and analyzed the effect of technological parameters on surface morphology and hardness. Xu M.S et al.^[16] studied the microstructure and properties of laser cladding Ni base alloy of 45 steel. Xu Q.K et al.^[17] studied the technicality of TiBCN powder CO₂ laser cladding on the surface of steel 45. Liu X.M et al.^[18] studied 45 steel laser cladding Ni35B+WC alloy and found that WC content can improve the hardness and wear resistance of cladding layer. The above studies show that the process parameters are the main factors affecting the morphology, microstructure, hardness distribution and wear resistance of the coating. However, there is little

literature on the cladding layer of 304L alloy on the surface of 45 steel by pulsed laser, and there is a lack of optimized process parameters. As a result, the 304L alloy powder is not widely used in remanufacturing and surface strengthening of mechanical parts.

In this paper, the process optimization of laser cladding 304L alloy powder on 45 steel surface is studied. Firstly, single-factor test and multi-factor orthogonal test are carried out to analyze the influence of each process factor on the morphology of single-pass cladding layer. Then the range analysis method is used to evaluate the significant order of the influence of each process parameter on the single-pass cladding morphology. Based on the orthogonal test results, multi-objective fuzzy comprehensive evaluation is carried out to find the comprehensive optimal combination of cladding process parameters. Finally, the stability of the synthetic optimal process is verified by the test of morphology and hardness^[19-21].

2. Orthogonal Experimental Design

2.1. Experimental equipment and materials

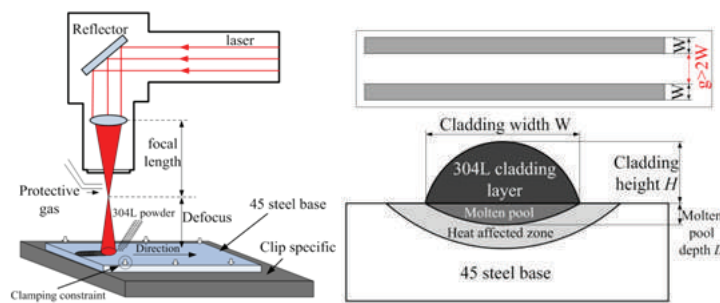


Figure 1. Schematic diagram of experimental principle of Laser cladding.

Table 1. Chemical composition of 304L stainless steel alloy powder and 45 steel substrate (wt%).

Materials	C	Si	Mn	Ni	Cr	P	S	Cu	O	Fe
304L alloy powder	≤0.03	≤1.0	≤0.2	8.0-12.0	18.0-20.0	-	-	-	≤0.15	Bal
45 steel	0.45	0.20	0.20	≤0.25	≤0.25	≤0.035	≤0.035	≤0.25	-	Bal

2.2. Design of experimental scheme

Due to the laser cladding machine used has many technological parameters and each parameter can be adjusted widely, the orthogonal experiment of multiple factors was carried out. The orthogonal experiment scheme $L_{16}(4^5)$ was designed, as shown in Table 2.

The macroscopic morphologies of 16 groups of single-pass cladding layers were obtained by orthogonal test, as

The Nd: YAG pulse laser cladding machine with a power of 800 watts is used in the experiment. The effective range of the cladding process parameters of the equipment: pulse current is 200A~ 230A, pulse width is 3.0ms~3.6ms, frequency is 14Hz~17Hz, defocusing amount is +8mm~+14mm, and scanning speed is 240mm/min~330mm/min. In order to avoid mutual influence of each channel of cladding and interference of residual heat of substrate, laser beams were scanned along the same direction during the test. The spacing g between adjacent cladding strips was set to be more than 2 times of the width W of single channel of cladding, and the scanning cooling interval was set to be 10 minutes. The experimental principle was shown in Figure 1.

The particle size of 304L stainless steel alloy powder is 180-320 mesh, the loose packing density is 3.8g / cm³, the base material is the 45 steel plate after being polished and cleaned, the length, width and height is 200mm×80mm×10mm. The mass fraction of 304L stainless steel alloy powder and 45 steel composition is shown in Table 1.

shown in Figure 2. From the macroscopic morphology, the width of no. 1-2 specimen is narrow and the cladding pattern is too dense. The surface roughness of no. 3-6 specimen is relatively large, and a few powder particles are in the state of semi-melting. There is un-melted powder and uneven cladding width on the surfaces of no.9, 11, 12, 14 and 16; The surface and edge of no. 7, 8, 10 and 15 cladding layers are smooth and have good macroscopic morphology.

Table 2. Multi-factor orthogonal experimental scheme ($L_{16}(4^5)$).

Number	Pulse current A	Pulse width ms	Pulse frequency Hz	Defocus distance mm	Scan velocity mm·min ⁻¹	Layer width mm	Layer height mm
1	200	3.0	14	+8	240	1.80	0.52
2	200	3.2	15	+10	270	2.12	0.38
3	200	3.4	16	+12	300	2.60	0.32

Number	Pulse current A	Pulse width ms	Pulse frequency Hz	Defocus distance mm	Scan velocity mm·min ⁻¹	Layer width mm	Layer height mm
4	200	3.6	17	+14	330	3.06	0.30
5	210	3.2	14	+14	300	2.32	0.58
6	210	3.0	15	+12	330	2.48	0.38
7	210	3.6	16	+10	240	2.66	0.54
8	210	3.4	17	+8	270	2.54	0.40
9	220	3.4	14	+10	330	2.36	0.32
10	220	3.6	15	+8	300	2.58	0.30
11	220	3.0	16	+14	270	2.92	0.56
12	220	3.2	17	+12	240	2.80	0.42
13	230	3.6	14	+12	270	2.86	0.38
14	230	3.4	15	+14	240	2.98	0.44
15	230	3.2	16	+8	330	2.54	0.30
16	230	3.0	17	+10	300	2.72	0.30

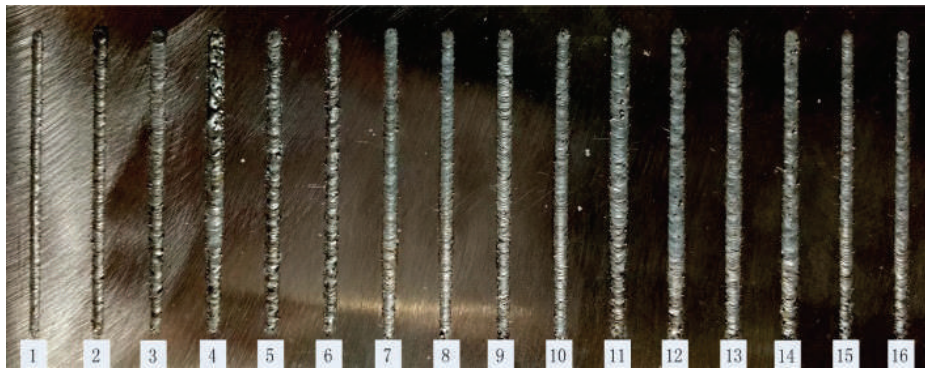


Figure 2. Multi-factor orthogonal experimental results.

3. Results and Discussion

3.1. Section morphology analysis

The cladding layer was cut along the direction perpendicular to the cladding, the cross section of cladding layer was observed by optical microscope, and the cross-section morphologies of 16 groups of samples were obtained, as

shown in Figure 3. As it can be seen from the figure, No. 1 cladding layer is height and narrow; No. 4, 9, 15 and 16 cladding layers are relatively flat, and the height and width do not meet the cladding requirements; No. 2, 6, 10 and 14 cladding layers are unevenly distributed and convex, and the cladding layer is not well fused; The surface of No. 3, 5, 7, 8, 11, 12 and 13 cladding layers is flat and has better height and width.

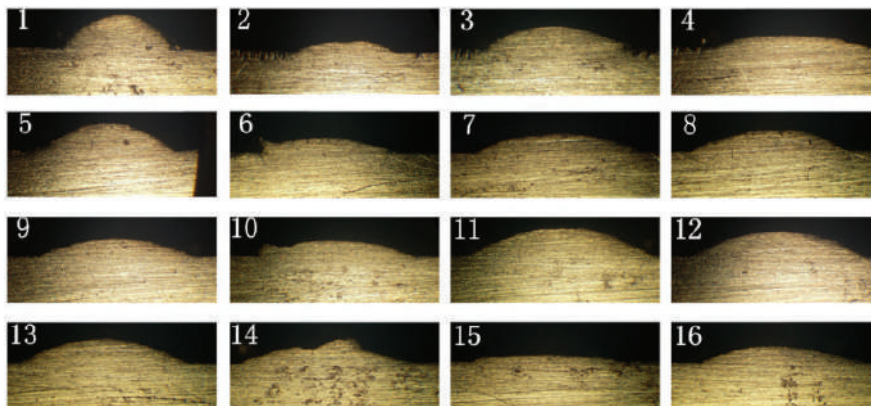


Figure 3. Cross-section microscopic image of a single laser cladding layer in orthogonal test.

3.2. Range analysis

Set T_{ij} be the sum of experimental results y_m (y_1 and y_2 are the width and height of cladding layer, respectively) at the level j in column i . K_{ij} is the experimental mean value at the j -th level of column i . R is the range value of column i , indicating the range of variation of the test index within the value range of this factor. $\max(K)$ and $\min(K)$ are the maximum and minimum K values in column i respectively. In formula (1), j is the number of levels, i is the number of columns, namely the number of factors (A, B, C, D, E), and r is the number of repeated tests at the same level in a certain factor.

$$\begin{cases} T_j = \sum_{m=1}^4 y_m \\ K_j = \frac{T_j}{r} \\ R = \max(K) - \min(K) \end{cases} \quad (1)$$

The range analysis can determine the primary and secondary factors that affect the experimental results. The large range indicates that the factor has a great influence on the experimental results, and it is the main factor. The small range indicates that this factor has a great influence on the experimental results, and it is a secondary factor.

The width and height of the cladding layer are measured by the microhardness tester, and the range analysis results of laser cladding test results are calculated by using formula (1), as shown in Table 3. It can be seen from the Table 4 that the main factor affecting the cladding layer width is scanning speed E, and the corresponding optimal combination is $A_4B_4C_4D_4E_2$. The main factor affecting the cladding layer height is also the scanning speed E, whose optimal combination is $A_2B_1C_1D_4E_1$. The effect of scanning speed on height and width of the cladding layer is the main factor, the focal length has a greater effect on the width of the cladding layer and the least effect on the height, and the effect of pulse width and frequency on the height and aspect ratio of the cladding layer is in the middle level.

Table 3. Range analysis.

Items		Pulse current Factor A	Pulse width Factor B	Pulse frequency Factor C	Defocus distance Factor D	Scan velocity Factor E
The width of the cladding layer mm	T_{i1}	9.58	9.92	9.34	9.46	10.24
	T_{i2}	10.00	9.78	10.16	9.86	10.44
	T_{i3}	10.66	10.48	10.72	10.74	10.22
	T_{i4}	11.10	11.16	11.12	11.28	10.44
	K_{i1}	2.40	2.48	2.34	2.36	2.56
	K_{i2}	2.50	2.45	2.54	2.47	2.61
	K_{i3}	2.67	2.62	2.68	2.69	2.55
	K_{i4}	2.78	2.79	2.78	2.82	2.61
	R	0.38	0.35	0.45	0.46	0.06
	The precedence order of the factors: D > C > A > B > E					
Optimization levels		A_4	B_4	C_4	D_4	E_2
Optimal combination		$A_4B_4C_4D_4E_2$				
The high of the cladding layer mm	T_{i1}	1.52	1.76	1.80	1.52	1.92
	T_{i2}	1.90	1.68	1.50	1.54	1.72
	T_{i3}	1.60	1.48	1.72	1.50	1.50
	T_{i4}	1.42	1.52	1.42	1.88	1.30
	K_{i1}	0.38	0.44	0.45	0.38	0.48
	K_{i2}	0.48	0.42	0.37	0.39	0.43
	K_{i3}	0.40	0.37	0.43	0.38	0.38
	K_{i4}	0.36	0.38	0.35	0.47	0.32
	R	0.12	0.07	0.10	0.09	0.16
	The precedence order of the factors: E > A > C > D > B					
Optimization levels		A_2	B_1	C_1	D_4	E_1
Optimal combination		$A_2B_1C_1D_4E_1$				

Range analysis cannot directly reflect the optimal results under the control of multiple indexes, and comprehensive evaluation is needed to determine the comprehensive optimal process parameter combination. Therefore, the surface height and width indexes of 304L laser cladding layer are comprehensively analyzed by fuzzy comprehensive evaluation method.

The specific methods of comprehensive analysis are:

Firstly, the fuzzy judgment matrix is obtained through the comment set of each sample factor set, and the weight judgment matrix of each evaluation index is obtained through expert knowledge and experience.

Then, the analytic hierarchy process (AHP) is used to analyze the weight consistency index and find the objective weight coefficient of each evaluation index.

Finally, fuzzy operator is used for fuzzy comprehensive evaluation.

The fuzzy comprehensive evaluation factor set: {cladding height, cladding width}, comment set: {good, relatively good, general, bad, poor}. The evaluation of cladding height \tilde{H}_i and cladding width \tilde{w}_i , obtained the fuzzy matrix \tilde{F}_i ($i=1,2,3...16$, Where i is the serial number of cladding strip), the first row of the matrix \tilde{F}_i values from \tilde{H}_i , and the second row values from \tilde{w}_i .

The *zadeh* operator is used to conduct compound operation on the fuzzy matrix to get the evaluation result \tilde{Z}_i , and the normalized processing is done \tilde{Z}^*_i ($i=1,2,3...16$), as shown in Table 4. As can be seen from Table 4, \tilde{Z}^*_7 and \tilde{Z}^*_8 should be the highest level, from the level of "good" quality, the comprehensive optimal result is \tilde{Z}^*_7 . In other words, the comprehensive optimal process parameters are current 210A, pulse width 3.6ms, frequency 16Hz, defocusing amount +10mm, and scanning speed 240mm/min.

Table 4. Evaluation results of fuzzy matrix.

$\tilde{Z}^*_1 = (0.14, 0.43, 0.29, 0.14, 0.00)$	$\tilde{Z}^*_2 = (0.10, 0.50, 0.40, 0.00, 0.00)$
$\tilde{Z}^*_3 = (0.00, 0.20, 0.40, 0.40, 0.00)$	$\tilde{Z}^*_4 = (0.00, 0.11, 0.22, 0.44, 0.22)$
$\tilde{Z}^*_5 = (0.00, 0.23, 0.31, 0.31, 0.15)$	$\tilde{Z}^*_6 = (0.00, 0.08, 0.46, 0.31, 0.15)$
$\tilde{Z}^*_7 = (0.42, 0.42, 0.17, 0.00, 0.00)$	$\tilde{Z}^*_8 = (0.36, 0.55, 0.09, 0.00, 0.00)$
$\tilde{Z}^*_9 = (0.30, 0.30, 0.40, 0.00, 0.00)$	$\tilde{Z}^*_{10} = (0.08, 0.25, 0.50, 0.17, 0.00)$
$\tilde{Z}^*_{11} = (0.09, 0.18, 0.55, 0.18, 0.00)$	$\tilde{Z}^*_{12} = (0.09, 0.18, 0.55, 0.18, 0.00)$
$\tilde{Z}^*_{13} = (0.00, 0.30, 0.60, 0.10, 0.00)$	$\tilde{Z}^*_{14} = (0.00, 0.10, 0.50, 0.40, 0.00)$
$\tilde{Z}^*_{15} = (0.00, 0.17, 0.42, 0.42, 0.00)$	$\tilde{Z}^*_{16} = (0.08, 0.23, 0.46, 0.31, 0.00)$

3.3. Hardness testing

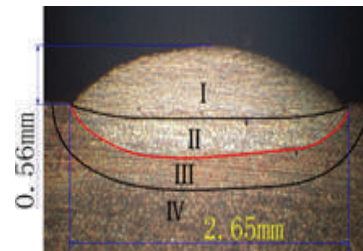
Through the results of fuzzy comprehensive evaluation, it can be found that when the scanning speed and defocus are controlled in the range of 240 ~ 270 mm/min and + 8 ~ 10 mm respectively, the cladding layer with better surface shape and no crack defects can be formed. Figure 4 (a) shows the three single-pass cladding morphologies under the optimal process parameters. It can be seen from the Figure 4 (a) that the surface of the cladding layer (No. 1, No. 2 and No. 3) is smooth and continuous, with uniform height and width, and good formation. The cladding width is 2.54mm, 2.56mm and 2.54mm, and the height is 0.56mm, 0.54mm and 0.54mm, respectively. Figure 4 (b) shows the cross section morphology of the cladding layer corroded by 4% nitric acid alcohol in No. 1. It can be seen that the cladding layer has a good bond with the substrate, and no cracks, pores and other defects are found.

The micro-hardness of the No. 1 cladding sample in Fig. 4b was observed, and 11 measuring points were set along the vertical direction on the section. The measuring point distribution in the cladding layer I molten pool II, IV, III heat-affected zone and the 45steel base IV, respectively (as shown in Figure 5 (a)). HV-1000 micro-hardness tester was used to measure the hardness of cladding samples (KGF =0.5), and the test results were shown in Figure 5 (b). By the figure shows, molten pool II has the highest hardness and as depth increases, the hardness of cladding layer I value is higher, but lower than the molten pool II matrix

IV minimum hardness, the hardness of heat affected zone III hardness value rapid transition from high to low hardness value, the final hardness is only slightly higher than the base material. Cladding layer I, molten pool II, heat affected zone III and IV average hardness are 406.2 HV_{0.5}, 470.8HV_{0.5}, 230.5HV_{0.5}, 202.0HV_{0.5}, respectively. The average hardness of the cladding layer I is 2.33 times of the 45 steel substrate IV.



(a)morphology



(b)the cross section shape.

Figure 4: Three single-pass cladding morphologies under the optimal process parameters

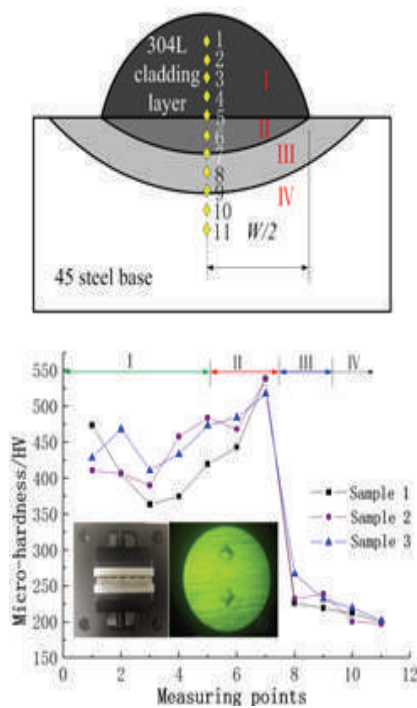


Figure 5. The micro-hardness of the cladding sample (a) position of measuring points;(b)hardness distribution curves.

Conclusions

The influence degree of different process parameters on the cladding layer morphology is found by range analysis of orthogonal test results. From the effect on cladding width, defocus distance $D >$ frequency $C >$ current $A >$ pulse width $B >$ scanning speed E . From the effect on cladding height, scanning speed $E >$ current $A >$ frequency $C >$ defocus distance $D >$ pulse width B . The scanning velocity E and defocus distance D are the most important factor affecting the cladding layer morphology.

The comprehensive optimal combination of cladding process parameters is current 210A, pulse width 3.6ms, frequency 16Hz, defocusing amount +10mm, scanning speed 240mm/min. The single pass cladding layer has good surface finish, stable width and height, good bonding between the cladding layer and the substrate, and no cracks, pores and other defects.

Under the comprehensive optimal process parameters, the average hardness of cladding layer, molten pool, heat affected zone and substrate is $406.2HV_{0.5}$, $470.8HV_{0.5}$, $230.5HV_{0.5}$ and $202.0HV_{0.5}$, respectively. The average micro-hardness of cladding layer is 2.33 times that of 45 steel substrate, and the surface hardness of the substrate after cladding is significantly improved.

Acknowledgements: This work was supported by the National Natural Science Foundation of China (No.51505268), Key project of shaanxi provincial science and technology department (2017ZDXM-GY-138) and Shaanxi provincial education department special research program (16JK1139).

References

- [1] C. Brunner-Schwera, T. Petrata, B. Grafa, et al.. High speed-plasma-laser-cladding of thin wear resistance coatings: A process approach as a hybrid metal deposition-technology [J]. Vacuum, 2019, 166 : 123-126.
- [2] E Govekar, A Jeromen, A Kuznetsov, et al.. Study of an annular laser beam based axially-fed powder cladding process [J]. CIRP Annals-Manufacturing Technology, 2018, 67: 241-244.
- [3] Guo W, Zhang Y P, Chai R X. Numerical Simulation and Experimental Study of Single-Track Laser Cladding of 304 Stainless Steels [J]. Laser & Optoelectronics Progress, 2019, 56(9): 091401-1-7.
- [4] Yu T B, Song B X, Xi W C. Influence of Laser Cladding Process Parameters on Morphology of Cladding Layer and Its Optimization [J]. Journal of Northeastern University (Natural Science), 2019, 40(4): 537-542.
- [5] Navas C, Conde A, Fernandez B J, et al.. Laser coatings to improve wear resistance of mouldsteel[J].Surface and Coatings Technology,2005,194(1):136-142.
- [6] Huang Y, Sun W L, Chen Y. Trajectory planning of laser cladding remanufacturing for complex shaft shaped part [J].Infrared and Laser Engineering,2017,46(5):0506005.
- [7] Wang H, Wang L W , Wang T, et al..Method and implementation of remanufacture and repair of aircraft engine damaged blades[J]. Acta Aeronautica et Astronautica Sinica,2016,37(3): 1036-1048.
- [8] Feng H,Li J F,Sun J. Study on Remanufacturing Repair of Damaged Crank Shaft Surface by Laser Cladding [J]. Chinese Journal of Lasers,2014,41(8): 0803003.
- [9] Liu F G, Lin X, Song K. Microstructure and Mechanical Properties of Laser Forming Repaired 300M Steel[J]. Acta Metallurgica Sinica,2017,53(3):325-334.
- [10] Xu B S, Fang J X, Dong S Y, et al..Heat-affected Zone Microstructure Evolution And Its Effects On Mechanical Properties For Laser Cladding FV520B Stainless Steel[J]. Acta Metallurgica Sinica, 2016,52(1):1-8.
- [11] Song M, Kan Y, Cheng Z H, et al..Study on Microstructure and Performance of Laser Cladding Layer on Ultra-high Strength Stainless Steel Surface[J].Hot Working Technology, 2017,46(6):148-151+154.
- [12] Parekh R, Buddu R K, Patel R I. Multiphysics Simulation of Laser Cladding Process to Study the Effect of Process Parameters on Clad Geometry [J]. Procedia Technology, 2016, 23: 529-536.
- [13] Jiao X Y, Wang J, Wang C M, et al..Effect of laser scanning speed on microstructure and wear properties of T15M cladding coating fabricated by laser cladding technology[J]. Optics and Lasers in Engineering,2018,110: 163-171.
- [14] Lei J F, Qi W J, Xie Y D, et al..Optimization of Process Parameters of Laser Cladding Ni60-25%WC Coating on

- U71Mn Steel[J].Surface Technology,2018,47(3):66-70.
- [15] Zan S P, Jiao J K, Zhang W W. Study on laser cladding process of 316L stainless steel power[J].Laser & Optoelectronics Progress,2016,6:061406.
- [16] Xu M S,Li J F ,Li H D, et al..Influence on Powders and Process Parameters on Bonding Shear Strength in Laser Cladding[J].Journal of Mechanical Engineering,2017,53(9): 209-216.
- [17] Xu Q K, Hu J D, Zhang W C. Application of TiBCN Powder as Additive in Laser Cladding of 45 Steel[J]. Applied Laser,2018,38(1):7-11.
- [18] Liu X M, Xie J J, Chen H. Manufacturing Stamping Die by Laser Cladding Ni35B+WC on the Surface of 45 Steel [J]. Rare Metal Materials and Engineering,2013,42(2):247-250.
- [19] Li B C, Zhao Y, Yu T B, et al.. Experimental Study of Single Pass Cladding Layers for Process Parameter Selection of Laser Cladding Ni204 Alloy [J]. Applied Laser,2018, 38(5):713-719.
- [20] B Bax, R Rajput, R Kellet, et al.. Systematic evaluation of process parameter maps for laser cladding and directed energy deposition [J]. Additive Manufacturing, 2018, 21: 487-494.
- [21] Li Y J, Dong S Y, Yan S X, et al.. Elimination of voids by laser remelting during laser cladding Ni based alloy on gray cast iron [J]. Optics and Laser Technology, 2019, 112: 30-38.

Study on the Cutting Temperature of the Textured Tool by 3D FEA Simulation

Siwen TANG^{1*}, Pengfei LIU¹, Rui WANG¹, Qiulin NIU², Guoqing YANG², Wenhui LIU³, Qian LIU⁴

1 Hunan Provincial Key Laboratory of Health Maintenance for Mechanical Equipment, Hunan University of Science and Technology, Xiangtan, China

2 Hunan Provincial Key Laboratory of High Efficiency and Precision Machining of Difficult-to-Cut Material, Hunan University of Science and Technology, Xiangtan, China

3 Hunan Provincial Key Defense Laboratory of High Temperature Wear Resisting Materials and Preparation Technology, Hunan University of Science and Technology, Xiangtan, China

4 Engineering Research Center of Advanced Mining Equipment, Ministry of Education, Hunan University of Science and Technology, Xiangtan, China

***Corresponding Author:** Siwen TANG, Hunan Provincial Key Laboratory of Health Maintenance for Mechanical Equipment, Hunan University of Science and Technology, Xiangtan, 411201, China

Abstract:

Temperature plays an important role in the life of cutting tools. However, it is sometimes difficult to observe instantaneously because of limited data acquisition, especially for the textured tool. In this paper, the performance of microgroove textured cutting tools for three-dimensional (3D) oblique dry turning of AISI 1045 steel was studied by finite element simulation. The effects of width, depth and spacing of strip micro-texture on cutting temperature and the effect of cutting speed on cutting temperature of strip micro-texture tool were studied. The results show that the maximum temperature of the tool and the tip temperature first increase and then decrease with the increase of micro-texture width. When the micro-texture depth increases, the maximum temperature and the tool tip temperature decrease first and then increase. The highest temperature and tip temperature of the tool gradually increase with the increase of micro-texture spacing. The highest temperature and tip temperature of the tool increase with the increase of cutting speed, feed speed and cutting depth. In addition, the effective mechanism of micro-texture parameter for the temperature was proposed. It provides profound guidance for optimizing the microstructure parameters and cutting process of cutting tools according to cutting temperature in this study. It also provides an effective and practical method for the design, innovation and development of micro-textured tools.

Keywords: Micro-textured cutting tool; FEM modeling; Cutting temperature; Cutting parameters

1. Introduction

Dry cutting has attracted attention in mounting numbers to the emphasis on environmental issues^[1]. However, high friction and strong adhesion of the dry cutting process reduce the life of the tool^[2-3]. Recent studies have shown that a micro-texture on the tool surface can effectively decrease cutting force and tool-chip contact length, thereby improving the performance of the tool^[4-6]. Many researchers studied the cutting mechanism of micro-texture by using the experimental and simulation methods. Xie et al.^[7] found the cutting forces for micro-grooved tool decreased 32.7% compared to traditional plane tools

while machining titanium alloys. Lei et al^[8] experimentally researched the performance of the micro-pool lubricated cutting tool in processing mild steel. Koshy and Tovey^[9] reported that texturing decreased the changeability of cutting forces during turning of hardening steel. Sugihara and Enomoto^[10] revealed that a cutting tool with micro-textured surface improved tool cutting performance (e.g., anti-adhesive properties) in wet and dry-cut aluminum alloy A5052. Obikawa and Kani^[11] found that the vertical and horizontal types of micro-texture could reduce cutting forces most effectively. Sun et al.^[12] studied the cutting performance of the hybrid texture self-lubricating

tool. The effects of these nanoscale surface textures with/without WS2 solid lubricant coatings comparing with the conventional investigated by Deng et al. [13] tools. Dong et al. [14] studied the effect of texture morphology, texture parameters on the cutting force and effective friction coefficient by using Deform 3D finite element simulations. However, there is less research on the temperature of the micro-texture tool since cutting temperature cannot be observed instantaneously because of limited data acquisition, especially for the oblique cutting. Meanwhile, finite element simulations provide an effective means for predicting the cutting temperature of the micro-texture tool. Therefore, this paper uses the commercial software ThirdWave AdvantEdge to establish a three-dimensional model of micro-textured tool cutting. Based on this model, the influence of micro-texture parameters on cutting temperature was studied, and the mechanism of influence of micro-texture parameters on cutting temperature was analyzed. The high model can be used to predict the temperature of the cutting process of the tool.

2. Establishment of Finite Element Model

2.1 Geometric model

The 3D FEM machining model are shown in Figure 1. The commercial software ThirdWave AdvantEdge has been used to simulate the cutting process. An oblique cutting model was established, the tool cutting edge angle $K_r=75^\circ$, as shown in Figure 1. Adaptive grid technology and updated Lagrangian finite element formula as well as continuous meshing are used in this model. The area of the tool and the workpiece closer to the tool-chip contacted area has fine mesh, which is beneficial to improve the simulation precision. The mesh far from the cutting region is coarser, which is convenient for the calculation, as shown in Figure 2. The parameter setting for mesh generation is illustrated in Figure 3. The workpiece material is 15 mm in diameter and the total cutting distance is 6 mm. The cutting tool is fixed during the cutting process, and the workpiece to do the rotary motion. The cutting conditions are given in Table 1. The initial simulated temperature is 20°C .

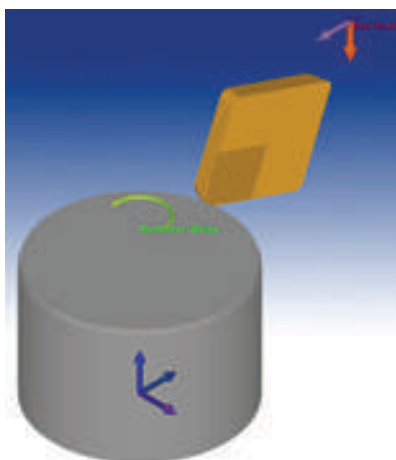


Figure 1. Finite element model

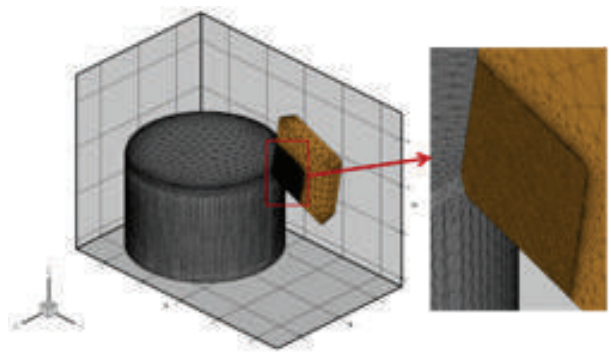


Figure 2. Mesh generation of FEM

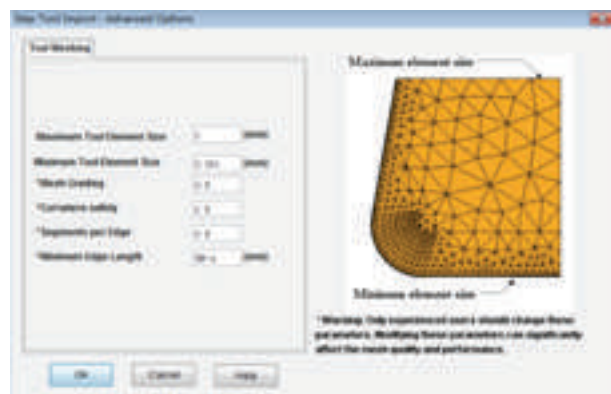


Figure 3. Parameter setting for mesh generation

Table 1. Cutting conditions

Parameters	Values
Cutting speed, $V(\text{m/min})$	90, 150, 210, 270, 330
Feed rate, $f(\text{mm/rev})$	0.05, 0.075, 0.1, 0.125, 0.15
Depth of cutting, $d(\text{mm})$	0.1, 0.2, 0.3, 0.4, 0.5

2.2 Cutting tool

The geometric model of the tool was established with Pro/E software. The tool size was $8\text{mm} \times 8\text{mm} \times 1.5\text{mm}$. Rake angle $\gamma_0=0^\circ$, clearance angle $\alpha_0=11^\circ$, cutting edge angle $K_r=75^\circ$, cutting edge inclination $\lambda_0=0^\circ$, corner radius $r_c=0.5\text{mm}$. The striped microstructure was built on the rake faces of the commercial Carbide-Grade-P cutting tool. The geometric model of the non-textured and textured tool is featured in Figure 4. Because the hardness of the tool is much greater than the hardness of the workpiece, the cutting time is short, and the tool wear is small during the cutting process. Therefore, the changes in the micro-texture geometry are not considered during the simulation cutting process. The MT-0, MT-90, MT-45, and MT-135 were named as micro-texture tools with a lot of grooves in the directions of horizontal (0°), vertical (90°) and slanting at 45° and 135° to the cutting edge on the rake faces. The parameter values of tiny grooves on the tool rake face are presented in Table 2. The micro-texture tool model established by Pro/E was imported into the Third Wave Advantage. Rake angle of

Tool $\gamma_0 = -6^\circ$, flank angle $\alpha_0 = 11^\circ$, and tool cutting edge inclination $\lambda_0 = 0^\circ$.

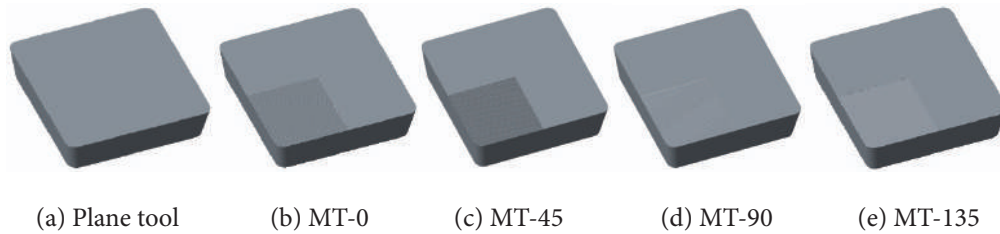


Figure 4. Geometry model of cutting tools

Table 2. Parameter values of micro-texture on tool rake face

Micro-textured cutting tool parameters	Values/ μm
Groove width	40, 60, 80, 100, 120, 150
Groove depth	5, 15, 25, 35, 45
Groove spacing	40, 80, 130, 180, 150, 300

2.3 Workpiece

The workpiece is AISI 1045 steel. The Johnson-Cook model is used to describe the thermo-viscoplastic deformation behavior of materials at high strain rates in this study. The model links the strain hardening effect, strain rate effect and thermal softening effect produced by materials at high strain rates. The specific form of the model is as follows:

$$\sigma = (A + B\varepsilon^n) \left[1 + C \ln \left(\frac{\dot{\varepsilon}}{\dot{\varepsilon}_0} \right) \right] \left[1 - \left(\frac{T - T_r}{T_m - T_r} \right)^m \right] \quad (1)$$

where σ is the effective yield stress, A is the yield strength, B is the strain hardening parameter, n is the hardening index, ε is the equivalent plastic strain, C is the strain rate strengthening parameter, $\dot{\varepsilon}$ is equivalent plastic strain rate, $\dot{\varepsilon}_0$ is the reference strain rate of the material, T is the operating temperature, T_{room} is the reference room temperature, T_{melt} is the melting point of the material, m is the thermal softening coefficient. Coulomb friction is used in AdvantEdge, which is as described the following equation: $F_f = \mu * F_n$, where F_n is a normal force applied between surfaces, μ refers to the coefficient of friction. F_f is the force produced by friction.

3. Experimental Validation

FEM model is validated by comparing with experimental results when $V=270\text{m/min}$, $f=0.1\text{mm/r}$ and $a_p=0.3\text{mm}$. In the experiments, all tools with or without texture are chosen for the cutting performance. The micro-texture width, groove depth, and groove spacing is $40\mu\text{m}$, $25\mu\text{m}$, and $40\mu\text{m}$, respectively. The machining conditions, tool condition and material are the same as in the simulation. The three directional cutting force in the X-, Y-, and Z-axes was measured by a dynamometer system consist of a Kister 9527B-type three-way piezoelectric dynamometer, a 5080-type charge amplifier, a PCIM-DAS1602/16-type data acquisition card, and a Dyno Ware System data acquisition system. The experimental and simulated cutting force, thrust force and feed force are depicted in Figure 5. All values of force are average in the figure. The results

show that all three cutting forces have good consistency between experiment and simulation. The differences between the experimental and emulational results for the three-dimensional force are all below 6%. It can be justified that the FEM model can accurately simulate the three-dimensional turning of AISI 1045 steel based on the comparisons as shown in Figure 5. In addition, the force and temperature of cutting are all affected by the same factor such as workpiece, cutting parameters, tool material and tool geometry. So, the established model can describe the effect of texture on the cutting temperature of the tools with and without texture.

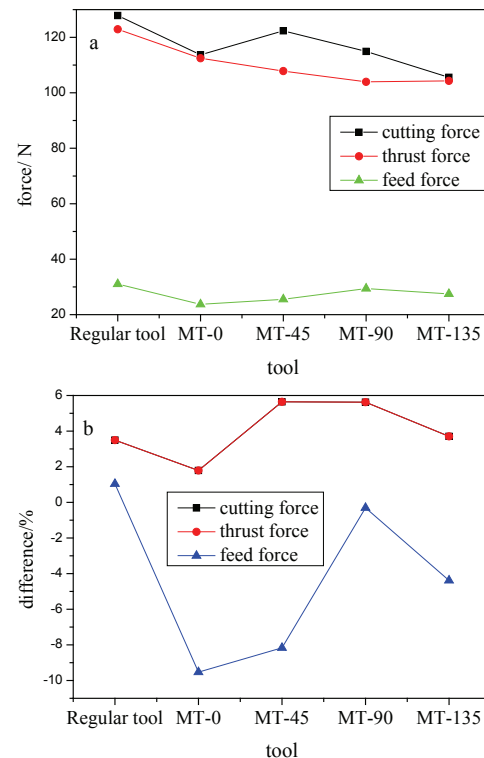


Figure 5: Cutting force of the experiment (a) and difference between the simulated and experimental cutting force (b). ($v_c=270\text{m/min}$, $f=0.1\text{mm/r}$, $a_p=0.3\text{mm}$)

4. Result and Discussion

4.1 Effect of morphological parameters on cutting temperature

The temperature distribution nephogram of the cutting tools with and without micro-texture cutting with AISI 1045 steel are shown in Figure 6. The cutting parameters are the same as section 2. The maximum temperature of the plane tool is at the tip of the tool and that of the tools with micro-texture appears at the ridge edge of the micro-texture. Because the microgrooves on the micro-texture of the tool surface can transfer cutting heat to the micro-texture direction faster, the edge of the micro-texture is in direct contact with the chip. So a large amount of cutting heat is concentrated on the edge of the micro-texture. It caused the highest temperature of the micro-texture tool to be distributed on the edge of the micro-texture. Besides, the micro-texture tool tools with different texture directions have different temperature distribution characteristics. Figure 7 shows the max temperature and the tip temperature of tools with and without micro-texture. Tools with micro-texture all decreased the cutting temperature to some extent compared to plane tools, especially for the tool MT-135. The maximum and the tip temperature of MT-135 were reduced by 10.4% and 13.2% compared to plane tools, respectively. In the texture tool, MT-45 has the highest cutting temperature, MT-90 second, MT-0 third, MT-135 minimum.

The flow direction of the chip is controlled by the microstructural shape on the rake face. Dong's research [14] shows that the tool has the lowest friction coefficient and the cutting force when the present of micro-texture

direction making the chip flow angle smaller. It can be observed the distribution of cutting temperature in Figure 6. It shows high-temperature area of MT-0 and MT-135 tool was significantly smaller than the MT-45, MT-90 and plane tool. It also shows that the two kinds of cutting tools in these cutting conditions is conducive to the reduction of tool cutting angle. So it helps reduce the tool and chip friction, cutting force and cutting temperature.

Wanigarathne et al. [15] studied the temperature of TiN / TiCN / TiC coated groove tool cutting with AISI1045 steel by infrared thermal imager. When $v_c = 200 \text{ m/min}$, $f = 0.15 \text{ mm/rev}$, the cutting temperature increases with the increase of cutting time, and the tool surface temperature increases from 350 to 500 °C during the cutting time of 50s ~ 65s. Song et al. [16] studied the cutting temperature of the micro-holes CaF₂ self-lubricating tool using an infrared thermal imager when cutting with AISI 1045 hardened steel. The research shows that the cutting temperature is from 400 ~ 550 °C at the speed range of 60 ~ 140m / min. Norouzifard et al. [17] measured the cutting temperature with an infrared thermal imager when using an ISO P30 tool cutting with AISI 1045 steel tool temperature at 503 °C to 662 °C, the cutting conditions are $v_c = 31.4 \sim 125.7 \text{ m/min}$, $f = 0.05 \sim 0.11 \text{ mm/rev}$. The processing conditions of this simulation study are different from those of the above experimental study, but the temperature range is consistent with the experimental results in general. At the same time, the cutting temperature of the micro-texture tool is slightly lower than that of the experiment due to the influence of the micro-texture on friction reduction. The comparison of the above experimental results shows that the cutting model established in this study can predict the temperature of the tool surface.

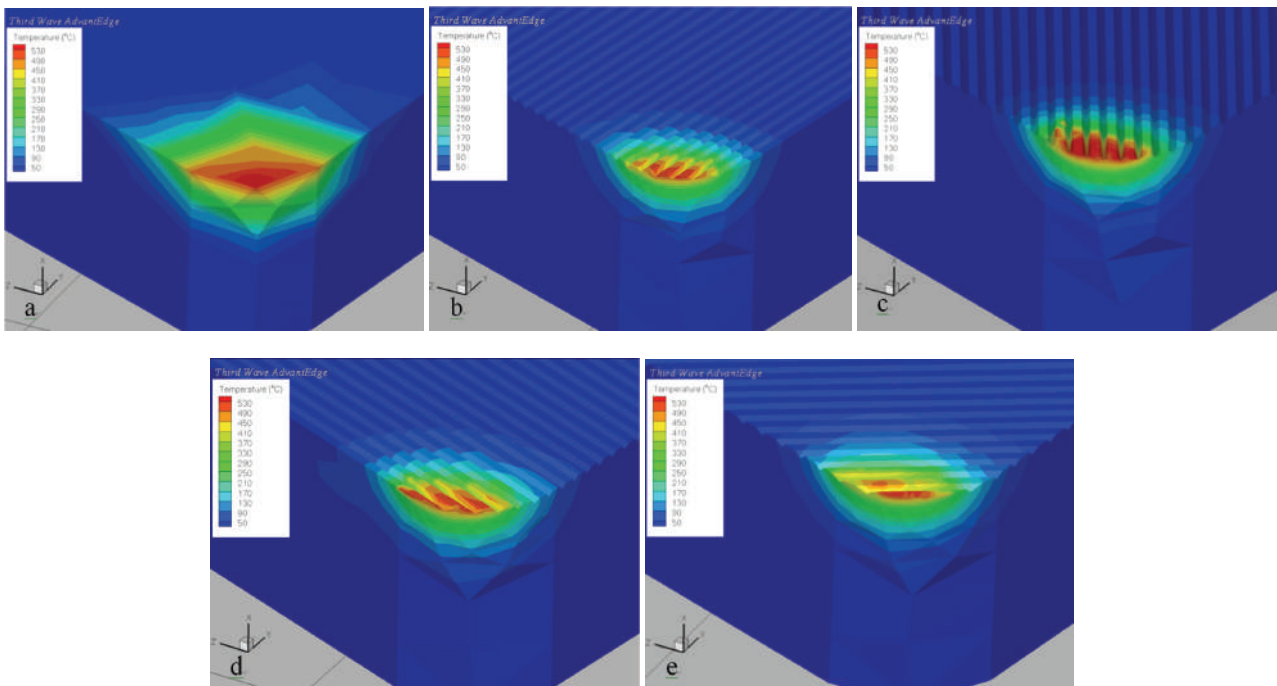


Figure 6. Cutting temperature distribution nephogram of different tool.

(a- plane tool, b-MT-0,c-MT-45,d-MT-90,e- MT-135, $v_c=270\text{m/min}$, $f=0.1\text{mm/r}$, $a_p=0.3\text{mm}$)

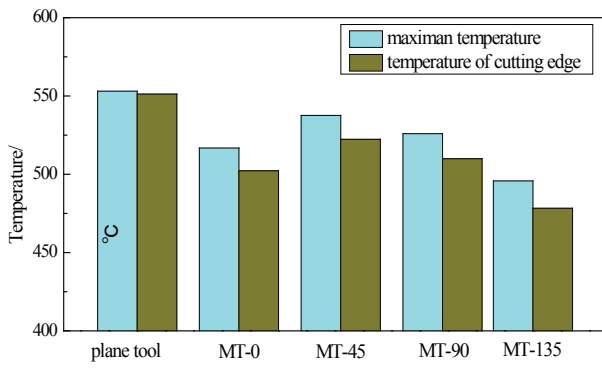


Figure 7. The maximum temperature and tip temperature of different tool.

4.2 Effect of microstructure size on cutting temperature

The MT-135 tool was picked to study the effects of width, depth, and pitch on the cutting temperature of micro-texture tools, as display in Figure 8. It can be found from the Figure 8 that the maximum temperature and the tip temperature of the tool increase first and then decrease with the increase of the micro-texture width. The maximum value appears at 80 μm . As the depth of the micro-texture increases, the maximum temperature and the tip temperature of the tool decrease first and then increase. And the tool has a lower temperature when the micro-texture depth is 25 μm . With the increase of the micro-texture spacing, the max temperature of the cutting tool and the tip temperature display an increasing trend.

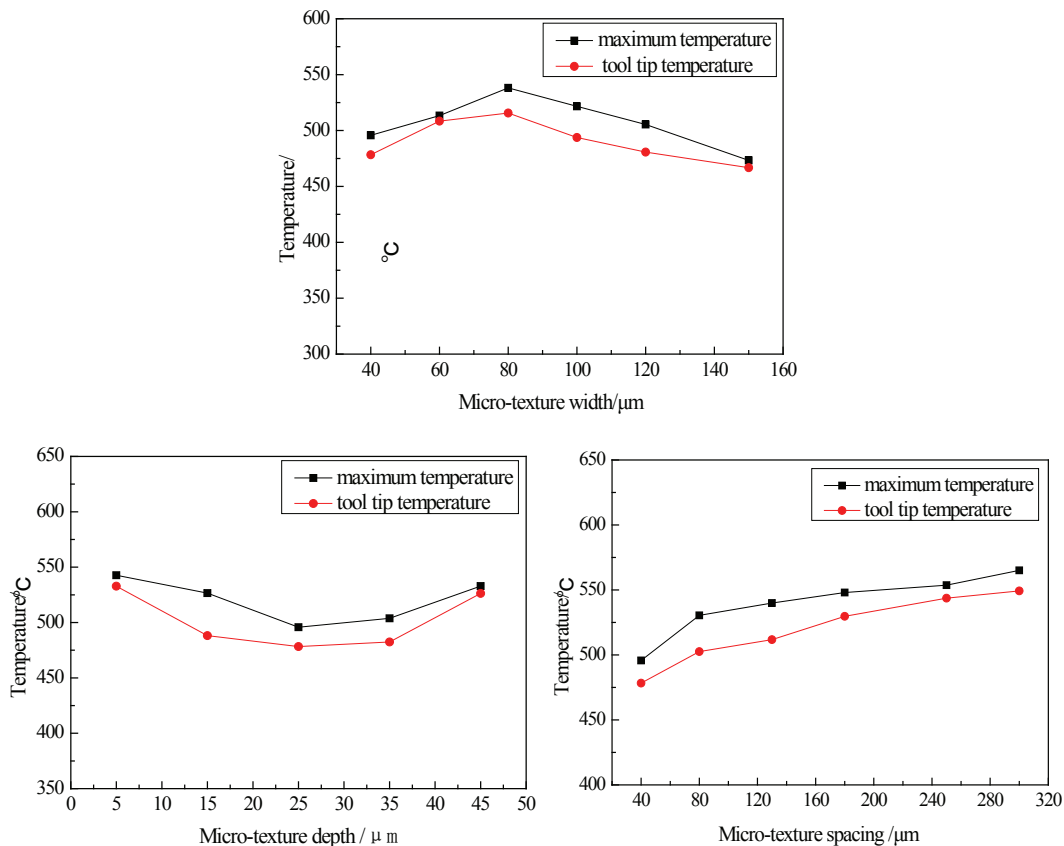


Figure 8. The effect of groove parameters on cutting temperature ($v_c=270\text{m/min}$, $f=0.1\text{mm/r}$, $a_p=0.3\text{mm}$)

During the cutting process, the texture supplies the space to reduce the contact between the chip and cutting tool, and then decrease the friction and the cutting tool temperature [13]. At the same time, the chips soften at high temperatures can enter the space of the micro-texture, and then cause a "derivative cutting" phenomenon [18]. This phenomenon reinforces the resistance of chip flows and the contact of the tool and chip, so the friction between the tool and chip increased, finally, making the tool temperature rise. According to the above analysis, it can be concluded that the new sources of cutting heat during the cutting were provided by the phenomena of secondary cutting. Micro-textured tool cutting diagram is shown in Figure 9.

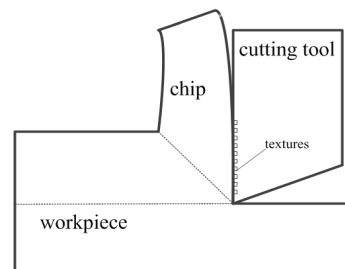


Figure 9. Schematic drawing of micro-textured tool cutting

Figure 10 is a schematic diagram showing the variation of micro texture width. When the micro-texture

width is small ($40\mu\text{m}$), the micro-texture provides a supremely fabulous contact interface to reduce the friction and temperature. Research^[19] shows that micro nano-scale texture is more effective than micro-scale texture because it minifies the contact region between the tool-chip interfaces. Yet as the micro-texture width increase ($40\sim 80\mu\text{m}$), the voids in the micro-texture increase, and the severer " derivative cutting" cause the rise of tool temperature. Furthermore, when the depth increases to a certain value ($>80\mu\text{m}$), the temperature decreased due to reduced contact is exceeding the temperature rise caused by the " derivative cutting" phenomenon, so the tool temperature reduced.

The micro-texture depth change is shown in Figure 11. When the micro-texture depth is small ($5\mu\text{m}$), the micro-texture is filled full of chips. At this condition, the

chip can flow as the plane tool. However, as the micro-texture depth increases ($5\sim 25\mu\text{m}$), the voids in the micro-texture increase. The temperature reduced due to reduced contact is over the temperature rise caused by the "secondary cutting" phenomenon, so the tool temperature decline. Nevertheless, when the depth raise to a certain value ($>25\mu\text{m}$), in the opposite case, the tool temperature increases sharply.

The micro-texture spacing is shown in Figure 12. With the increase of micro-texture spacing, the max temperature and the tip temperature of the cutting tool emerge an increasing trend. This is because the larger spacing, the less number of micro-textures involved in the cutting, so that the actual tool-chip contacts region expands, so the friction generated more heat. It causes the cutting temperature to rise.

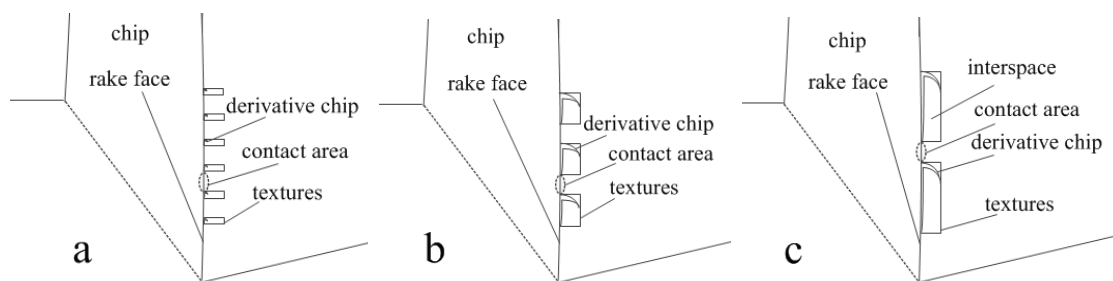


Figure 10. Is a schematic diagram of the micro-texture width change.

(a-micro-texture width is $40\mu\text{m}$, b-micro-texture width is $40\sim 80\mu\text{m}$, c-micro-texture width is greater than $80\mu\text{m}$)

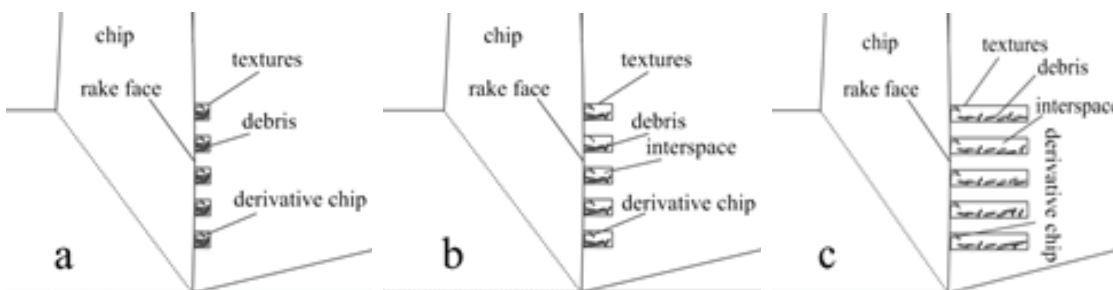


Figure 11. Schematic diagram of micro-texture depth change

(a-micro-texture depth is less than $5\mu\text{m}$, b-micro-texture depth is $5\sim 25\mu\text{m}$, c-micro-texture depth is greater than $25\mu\text{m}$)

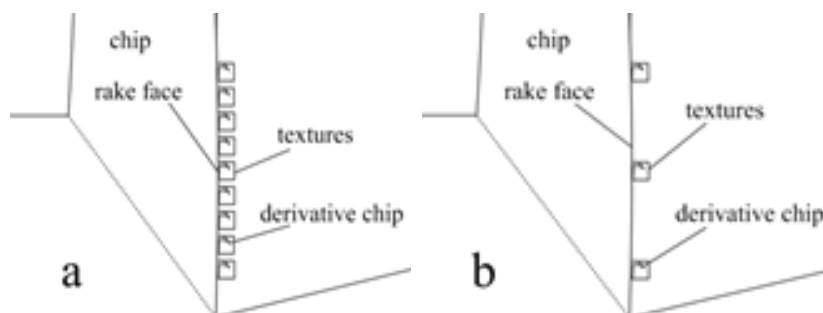


Figure 12. Schematic diagram of micro-texture spacing

(a-micro-texture spacing is small, b-micro-texture spacing is large)

4.3. Effect of cutting parameters on cutting temperature

Figure 13 shows the influence of cutting parameters on cutting temperature of the MT-135 tool with a width of 40 μm , a depth of 25 μm and a space of 40 μm . Under the same

feed and cutting depth, the maximum temperature and the tip temperature of the tool increase with the cutting speed go up. The effect of the feed rates and depth of cutting is also true.

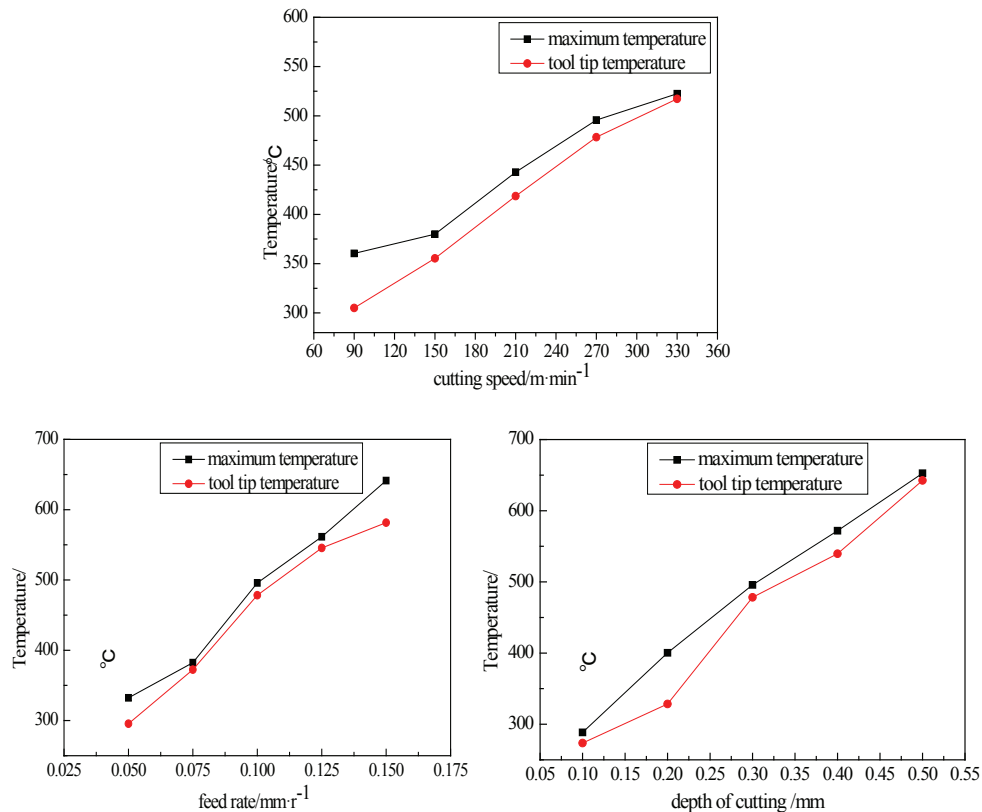


Figure 13. Effect of cutting parameters on cutting temperature

Conclusion

The micro-texture tool has good cutting performance and is used for cutting hard-to-machine materials. The finite element simulation technology is used to study the influence of micro-texture parameters of micro-texture tools on cutting temperature, which reduces the experimental cost and makes it easier to analyze the cutting performance of micro-texture tools, thus making it possible to prepare micro-texture tools with excellent performance, which is of great significance to the development of new tools. The finite element analysis model of the oblique cutting process of the surface micro-texture tool was established by using a FEM simulation. The effect of micro-texture morphology, size parameters and cutting parameters on the cutting temperature of micro-texture was studied with AISI 1045 steel. The main conclusions are as follows.

(1) All the micro-texture tools can diminish cutting temperature to some extent compared with the traditional tool. MT-135 tool has the lowest cutting temperature.

(2) The maximum temperature of the plane tool is at the tip of the tool and that of the tools with micro-texture emerges at the upper edge of the micro-texture. The maximum temperature and the tip temperature of the tool increase first and then reduced with the rise of the width of the

micro-texture. When the micro-texture depth increases, the maximum temperature and the tool tip temperature decrease first and then increase the maximum temperature and the tool tip temperature of the tool are gradually growing with the augment of micro-texture spacing.

(3) The maximum temperature of the tool and the tip temperature increase with the increase of cutting speed, feed rate and depth of cutting.

Acknowledgement: This work was financially supported by the National Natural Science Foundation of China (grant no. 51305134), a Project Supported by Scientific Research Fund of Hunan Provincial Education Department (grant no. 18B230) and Chinese Green Manufacturing System Integration Project (2017).

References

- [1] Sharma V, Pandey P M. Recent advances in turning with textured cutting tools: A review [J]. *Journal of Cleaner Production*. 2016, 137: 701-715.
- [2] Sreejith P S, Ngoi B K A. Dry machining: Machining of the future [J]. 2000, 101(1): 287-291.
- [3] Weinert K, Inasaki I, Sutherland J W, et al. Dry Machining and Minimum Quantity Lubrication [J]. *CIRP Annals* -

- Manufacturing Technology. 2004, 53(2): 511-537.
- [4] Wu Z, Deng J, Su C, et al. Performance of the micro-texture self-lubricating and pulsating heat pipe self-cooling tools in dry cutting process[J]. International Journal of Refractory Metals and Hard Materials. 2014, 45: 238-248.
- [5] Xie J, Luo M, He J, et al. Micro-grinding of micro-groove array on tool rake surface for dry cutting of titanium alloy [J]. International Journal of Precision Engineering and Manufacturing. 2012, 13(10): 1845-1852.
- [6] Xing Y, Deng J, Zhao J, et al. Cutting performance and wear mechanism of nanoscale and microscale textured Al₂O₃/TiC ceramic tools in dry cutting of hardened steel[J]. International Journal of Refractory Metals and Hard Materials. 2014, 43: 46-58.
- [7] Xie J, Luo M J, Wu K K, et al. Experimental study on cutting temperature and cutting force in dry turning of titanium alloy using a non-coated micro-grooved tool. International Journal of Machine Tools and Manufacture [J]. International Journal of Machine Tools and Manufacture. 2013, 73: 25-36.
- [8] Lei S, Devarajan S, Chang Z. A study of micropool lubricated cutting tool in machining of mild steel [J]. Journal of Materials Processing Technology. 2009, 209(3): 1612-1620.
- [9] Koshy P, Tovey J. Performance of electrical discharge textured cutting tools [J]. CIRP Annals - Manufacturing Technology. 2011, 60(1): 153-156.
- [10] Sugihara T, Enomoto T. Improving anti-adhesion in aluminum alloy cutting by micro stripe texture [J]. Precision Engineering. 2012, 36(2): 229-237.
- [11] Obikawa T, Kamio A, Takaoka H, et al. Micro-texture at the coated tool face for high performance cutting [J]. International Journal of Machine Tools and Manufacture. 2011, 51(12): 966-972.
- [12] Sun J, Zhou Y, Deng J, et al. Effect of hybrid texture combining micro-pits and micro-grooves on cutting performance of WC/Co-based tools [J]. The International Journal of Advanced Manufacturing Technology. 2016, 86(9-12): 3383-3394.
- [13] Deng J, Lian Y, Wu Z, et al. Performance of femtosecond laser-textured cutting tools deposited with WS₂ solid lubricant coatings [J]. Surface and Coatings Technology. 2013, 222: 135-143.
- [14] Kim D M, Bajpai V, Kim B H, et al. Finite element modeling of hard turning process via a micro-textured tool [J]. The International Journal of Advanced Manufacturing Technology. 2015, 78(9-12): 1393-1405.
- [15] Wanigarathne P C, Kardekar A D, Dillon O W, et al. Progressive tool-wear in machining with coated grooved tools and its correlation with cutting temperature[J]. Wear. 2005, 259(7): 1215-1224.
- [16] Song W, Deng J, Zhang X, et al. Experimental study on the cutting temperature of cemented carbides tool embedded with CaF₂ solid lubricants [C]. 2nd International Conference on Architectural, Civil and Hydraulics Engineering, 2016.
- [17] Norouzfard V, Hamed M. Experimental determination of the tool-chip thermal contact conductance in machining process [J]. International Journal of Machine Tools and Manufacture. 2014, 84(Supplement C): 45-57.
- [18] Duan R, Deng J, Ai X, et al. Experimental assessment of derivative cutting of micro-textured tools in dry cutting of medium carbon steels [J]. International Journal of Advanced Manufacturing Technology, 2017, 92(9-12).
- [19] Zhang K, Deng J, Sun J, et al. Effect of micro/nano-scale textures on anti-adhesive wear properties of WC/Co-based TiAlN coated tools in AISI 316 austenitic stainless steel cutting [J]. Applied Surface Science. 2015, 355: 602-614.

Effect of Microstructures and Mechanical Properties of Large Deformation High Entropy Alloy CoCrCuFeNi in Semi-solid Isothermal Heat Treatment

Lajie WANG¹, Jiao XIONG¹, Jun LIU^{2,3}, X J YANG^{1,2,3*}

¹ Gongqing College, Nanchang University, Nanchang, China

² School of Mechanical and Electrical Engineering, Nanchang University, Nanchang, China

³ Key Laboratory of Near Net Forming in Jiangxi Province, Nanchang, China

*Corresponding Author: X J YANG, School of Mechanical and Electrical Engineering, Nanchang University, 330031, China

Abstract:

The semi-solid slurries of the CoCrCuFeNi high entropy alloy (HEA) were fabricated through the recrystallization and partial melting (RAP) process by cold-rolling and partial remelting. The temperature range of the semi-solid region and the relationship between the liquid fraction and the temperature were determined by the differential scanning calorimetry (DSC) curve. The effect of isothermal temperature and holding time on the evolution of the microstructure and mechanical properties of the rolled samples was analyzed. The results show that the microstructure was significantly deformed, and the tensile strength has been increased by 107% after 63% rolling deformation of the CoCrCuFeNi high entropy alloy (HEA). The high-entropy alloy after cold rolling was maintained at 1150 and 1300 °C for 20, 30, 60, and 120 minutes respectively, the plasticity has been improved compared with the rolled high entropy alloy. The optimal plasticity was reached 13.7% and 7.9% at 1150 °C and 1300°C for 30 minutes, respectively. After semi-solid isothermal heat treatment, the grain morphology changed from dendritic of as-cast or rolled to spherulite and the grain size increased significantly with time and the holding temperature increased.

Keywords: high entropy alloy; plastic deformation; semi-solid isothermal treatment; tensile strength; microstructure

1. Introduction

As a new alloy design concept, high-entropy alloy (HEA) has attracted much attention of many researchers in recent years. Different from the traditional concept of single-element based alloy, HEAs are the multi-component alloys with equimolar or near-equimolar compositions^[1,2]. Therefore, high-entropy alloy is also known as multi-principal component high entropy alloy. Huang et al.^[3] have prepared high entropy alloy AlCoCrCu_{0.5}NiFe on single crystal silicon and glass by magnetron sputtering, which expanded the application prospect of high entropy alloy in terms of oxide film. Chen et al.^[4] manufactured Al_{0.25}CoCrFe_{1.25}Ni_{1.25} HEA coating on 45 steel surface by laser cladding, the results show that the surface hardness of cladding layer can reach 3.2 times of 45 steel due to the mutual solubility of high entropy alloy elements, the solution strengthening effect is produced. Qiu Jingwen, Fu Zhengfan^[5] et al. prepared high entropy alloy reinforced AZ91D composite by laser cladding, which greatly

improved the hardness and wear resistance of magnesium alloy, and better applied in aerospace, chemical industry, vehicles and biomedical fields. Therefore, HEA was regarded as a promising structural material. In order to further improve the mechanical properties of HEA, many researchers used spark plasma sintering^[6], high-pressure torsion^[7] and equal channel angular extrusion^[8] to obtain high-strength HEA.

The semi-solid metal process (SSM), as the most promising material-forming process in the 21st century, combined with the advantages of solidification and plastic processing, such as the good flowing ability, low resistance to deformation, and easy formation of complex and high precision parts^[9,10]. The key to the SSM process is to obtain a semisolid slurry with a uniform, small non-dendritic structure. The required spherical microstructure can be generated by either a liquid or a solid route. Solid-state path ways include strain induced melt activation (SIMA) method and recrystallization and partial melting (RAP)

method [11]. Some researchers have studied the effects of plastic deformation, isothermal temperature and holding time in an appropriate semi-solid temperature range on the microstructure evolution and tensile properties of A380 aluminum alloy through SIMA and RAP methods [12]. Chen et al. [13] pointed out that the SIMA process can produce ideal, fine semisolid tissues, in which spherical α -Mg particles have almost no residual liquid. The relationship between the spheroidization degree, holding time and liquid fraction in isothermal treatment is also discussed. However, the research focuses on the low melting point of Al and Mg alloys, there are few reports on high melting point alloys, especially for HEA. Rogal [14] obtained the spherical microstructure of CoCrCuFeNi HEA required for the thixotropic process through RAP method. However, the influence of semisolid conditions (isothermal temperature and time) on microstructure evolution, mechanical properties and coarsening mechanism is not given. These explorations will be interesting and meaningful, which will expand the understanding and application of HEA.

A two-phase FCC CoCrCuFeNi HEA was selected in this paper. Semi-solid slurry is produced by the RAP process through cold rolling and partial remelting. The microstructures and mechanical properties of cast, rolled and semisolid isothermal heat treatment alloys were studied. And the influence of isothermal temperature and holding time on microstructure evolution and tensile properties at room temperature were discussed.

2. Experimental Procedures

In this experiment, five high-purity metals (Co, Cr, Cu, Fe and Ni) with higher than 99.9% (mass fraction) purity were selected as raw materials. Each element is weighed according to the equal molar ratio, with a total weight of 4 kg. CoCrCuFeNi high entropy alloy was obtained by melting in a vacuum suspension induction melting furnace protected by high purity argon. In the smelting process, the ingot was re-melted 4-5 times to ensure uniform smelting. The cylinder sample with a dimension of 90 mm in diameter and 70 mm in height was obtained.

The rectangular sample with a dimension of 70 mm×15mm×6 mm was cut from the as-cast button. Large deformation rolling high entropy alloy sheet with a thickness of 2.2mm was obtained by 8 passes of rolling treatment, in which the first 7 passes rolling reduction are all 0.5mm, and the last pass rolling reduction is 0.3mm. The rolled plate is cleaned with anhydrous ethanol and then vacuum sealed with quartz tube. The quartz tube is kept flat and put into YFFG40/13G-YC three-phase resistance furnace for semi-solid isothermal treatment and water quenching after treatment at different temperatures and holding times.

The microstructure was investigated by X-ray diffraction (XRD) with the CuK α radiation and optical microscope (OM). The compositions of phase were analyzed by energy dispersive spectroscope (EDS). The thermal analysis was performed by the differential-scanning calorimetry (DSC) with a constant heating rate

of 20 K/min. The mechanical properties were characterized by tensile behavior. The tensile samples with a total length of 60mm, a thickness of 2.2mm, a clamping end width of 15mm, a standard tensile distance of 30mm, a section width of 5mm and a radius of 5mm arc transition as shown in Figure1.

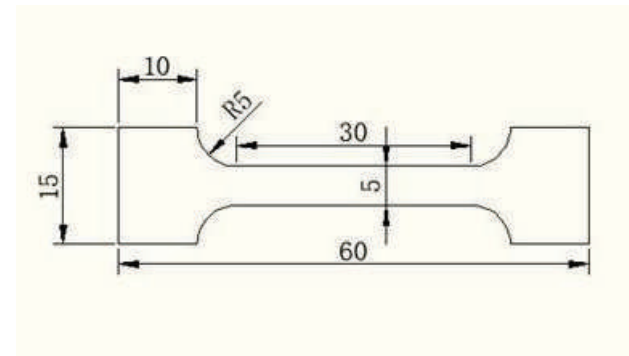


Figure1. Dimensional drawing of tensile samples (mm).

3. Results and Discussions

3.1. SEM of as-cast materials and thermodynamic results

The as-cast CoCrCuFeNi HEA has typical dendrite (DR) and interdendrite (ID) structures as shown in Figure 2. The chemical compositions of different phases were determined by SEM energy dispersion spectrometer (EDS) at the points of dendrite (DR) and interdendrite (ID) respectively. The DR structure was FCC2 matrix phase with high volume fraction. In the DR region, the ID phase with a low volume fraction is FCC1 phase. The chemical composition of FCC1 and FCC2 phases indicates that FCC1 phase is Cu rich phase. However, the concentration of Co Cr, Fe and Ni in FCC2 is similar as shown in Table 1. The reason leading to a strong segregation of Cu in the FCC1 phase from the EDS results is the positive mixing enthalpy of Cu-Cr, Cu-Co, Cu-Fe, and Cu-Ni^[15]. The volume fraction of the FCC2 phase was about 87%.

Figure 3 shows the DSC curves of as-cast and rolled CoCrCuFeNi HEA. There are two exothermic peaks in the as-cast alloy and the rolled alloy, and the positions of the exothermic peaks are basically the same, which indicates that the internal composition of the alloy has not changed after rolling. The first exothermic peak appears at about 1114 °C, the integral area of the peak is small and the temperature point is close to the melting point of copper (1083 °C). Combining DSC curve, EDS test and volume fraction calculation results, it could be judged that this peak represented FCC1 phase, and the second peak represented FCC2 phase. The alloy began to melt partially at about 1114°C and the crystal structure changed, the second exothermic peak appeared at about 1343°C and ended at about 1388°C, indicating that the alloy was completely melted at this time. The semi-solid holding temperature of the as cast sample is obtained by integrating the DSC curve in Figure 3. In the liquidus rate curve as shown in Figure 4, the liquidus rate is about 9.2% at 1150 °C, which is

relatively low, and there is a rapid increase of liquid phase ratio before 1150 °C. In combination with DSC curves, the FCC1 phase has been completely melted at 1150 °C, and the liquid phase ratio increases slowly with the increase of temperature. When the temperature reached 1350 °C, the liquid phase ratio curve increased rapidly, indicating that the FCC2 phase began to melt, and the liquid phase ratio approached 60%. It is very difficult to get accurate liquid phase ratio in the two regions where the liquid phase ratio changes rapidly, finally the liquid phase ratio changes rapidly and the solid phase ratio is easy to lose stability. When the temperature is higher than 1350 °C, the melting of FCC2 phase leads to the high liquid ratio of materials, which is easy to cause the deformation and melting and cannot maintain the macroscopic structure of the sheet metal during the semi-solid heat preservation treatment. Therefore, the semi-solid treatment temperature should be between 1133 °C and 1343 °C. Therefore, in this experiment, 1150 °C with a liquid phase ratio of 9.2% and 1300 °C with a liquid phase ratio of about 41% were selected as semi-solid insulation temperature.

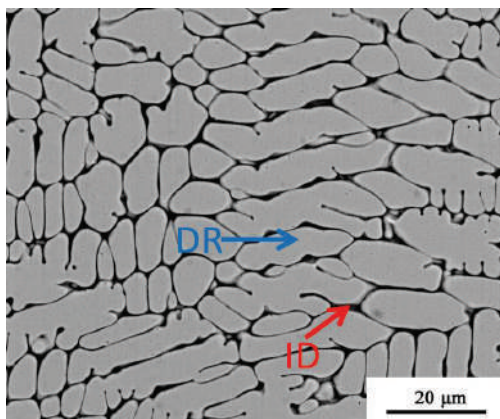


Figure 2: The SEM of as-cast sample.

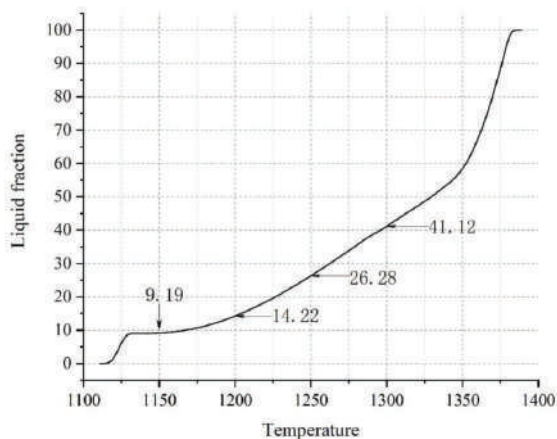


Figure 4: Liquid phase ratio curve of as-cast.

Table 1. Contents of each element at two regional points in the as-cast microstructure of CoCrCuFeNi high-entropy alloy (wt. %).

Sampling point	Co (%)	Cr (%)	Cu (%)	Fe (%)	Ni (%)
DR region	23.89	21.57	11.66	21.63	21.25
ID region	9.81	10.36	56.03	10.04	13.76

3.2. XRD diffraction

Figure 5 shows the X-ray diffraction patterns of samples in different states. Comparison before and after semi-solid isothermal treatment, the positions of each diffraction peak did not shift, and they were all combinations of FCC1 phase and FCC2 phase. The phase composition structure of CoCrCuFeNi high-entropy alloy did not change, indicating that CoCrCuFeNi high-entropy alloy had good thermal stability. In the subsequent analysis, the changes in material properties could be excluded the factors of phase structure change.

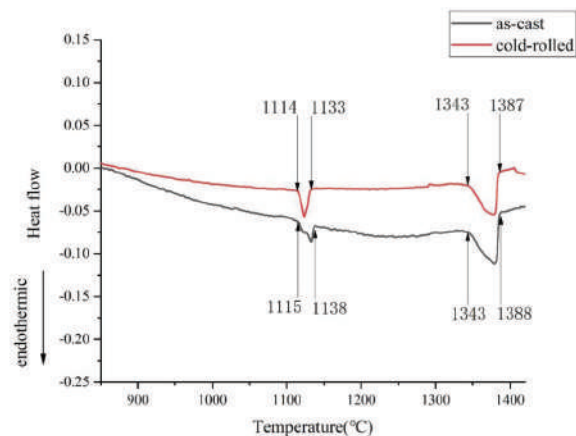


Figure 3. DSC curves of as-cast and rolled CoCrCuFeNi HEA.

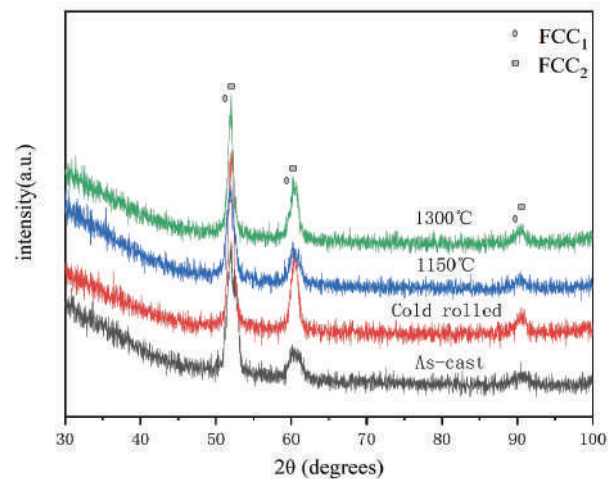


Figure 5: X-ray diffraction patterns of samples in different states.

3.3. Microstructure

As shown in Figure 6, the (a) and (b) are the metallographic diagrams of ingots in different areas, (a) is the upper ends of all the stretch sheet areas cut on the ingots, i.e the clamping area of the stretch sheet, (b) is the central area of the ingot, where the basic stretch sheet deformation area. The dendrite size in (b) region is more uniform and smaller than (a), which makes the tensile effect more stable. (c) shows the microstructure of the parallel rolling direction of the rolled plate. Compared with the as cast structure, it can be seen that the dendrites have obvious deformation, the secondary dendrite arm spacing is reduced, the dendrites have bending deformation, and even have dendrite fracture. (d) shows the microstructure in the vertical direction of

rolling. Compared with as cast samples, dendrites also have obvious extrusion deformation. (c) and (d) show that rolling makes the microstructure of the plate have a very large internal stress that can promote the grain boundary remelting in the semi-solid isothermal treatment, there are also a lot of dislocation energy in the crystal. (e) and (f) were the microstructure of the semi-solid isothermal treatment at 1150°C for 120min and 1300°C for 120 min respectively. Compared with the as-cast and rolled state, the morphology changed from dendrite to spherulite, and the grain size became smaller and evenly distributed, which indicated that the internal stress had been basically released. The higher the temperature of semi-solid isothermal treatment is, the larger the manager size is.

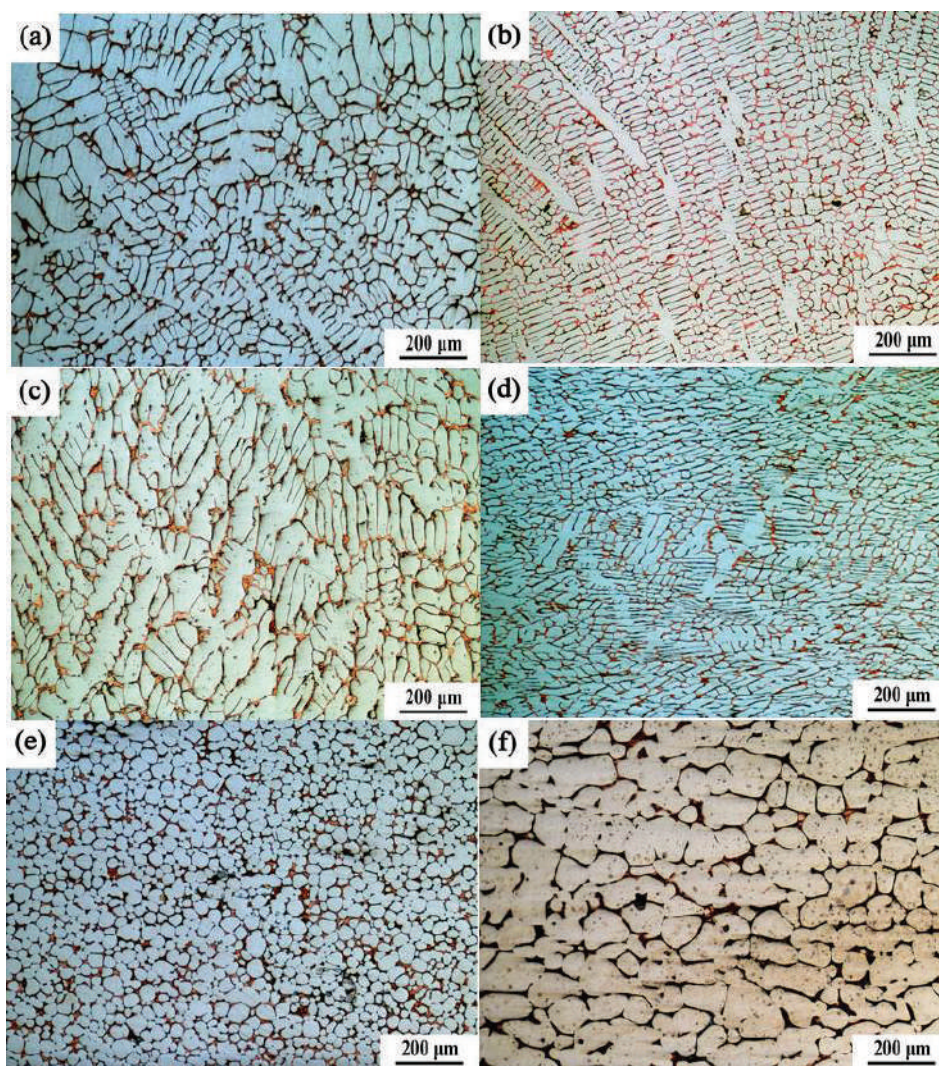


Figure 6. Metallographic photograph: (a) the upper area of the ingot;(b) central region of the ingot (c) parallel rolling direction (d) vertical rolling direction (e) 1150°C, 120min;(f) 1300°C, 120min.

Figure 7 shows the metallographic structure photos of semi-solid isothermal treated CoCrCuFeNi high-entropy alloy. The upper side(a), (c), (e) and (g) are the microstructure treated at 1150°C for 20min, 30min, 60min and 120min respectively, while bottom column (b), (d), (f) and (h) are the microstructure treated at 1300°C for 20min,

30min, 60min and 120min respectively. At 1150°C for 20 minutes, the grain size of FCC2 phase is still relatively small, the morphology and size of primary dendrite remain unchanged, and the secondary dendrite was partially remelted and peeled off to form small spherulites. For 30 minutes, the number of spherulites increased gradually and

the primary dendrite dissolved and fractured. When the temperature of semi-solid isothermal treatment is 1300 °C, the grain size increases obviously, and with the increase of treatment time, the larger the grain size is.

It can be seen that at 1150 °C or 1300 °C, the distribution of grains is uniform and the grain size is small when the time of semi-solid isothermal treat is 30 minutes. After 30 minutes, the grains grow with the increase of holding time; The average grain diameter is 50 μm and 180 μm at 1150 °C and 1300 °C for 120 minutes respectively, which indicated that the temperature has a key effect on grain growth.

The variation of grain size can be explained by growth kinetics. In the RAP process of manufacturing CoCrCuFeNi HEA semi-solid slurry, remelting heat provides energy to support dendrite fuse and spheroidization, while pre deformation stores internal energy. During reheating, recrystallization occurs, and with the formation of liquid phase, spherical grains are easy to form. Driving force of solid recrystallization is produced by the reduction of free energy due to the reduction of elastic storage energy (i.e. bit error energy)^[16]. During the whole isothermal process

of semi-solid remelting, the sharp angle of solid-state FCC2 grains is engulfed by the liquid phase first, and then the grains become larger and rounder.

3.4. Tensile properties

Figure 8 shows the stress-strain curves of as-cast and rolled alloys. As you can see, the mechanical properties of the alloy has significant improvement after rolling compared to as-cast alloy, Tensile strength increased from 455MPa to 945MPa, and Young's modulus is also greatly improved, which in accordance with the previous rolling sample that causes the lattice fracture and grain refinement of the alloy to increase the strength and hardness. However, the elongation after fracture is much lower than that of as cast alloy, which may be due to: (1) Severe plastic deformation causes lattice fracture, grain refinement makes the strength of the alloy increase significantly and decrease the plasticity; (2) Rolling treatment leads to a certain degree of stress concentration in the alloy, which causes some defects, such as cracks, etc., in the process of drawing, which makes the alloy fracture rapidly and leads to low elongation.

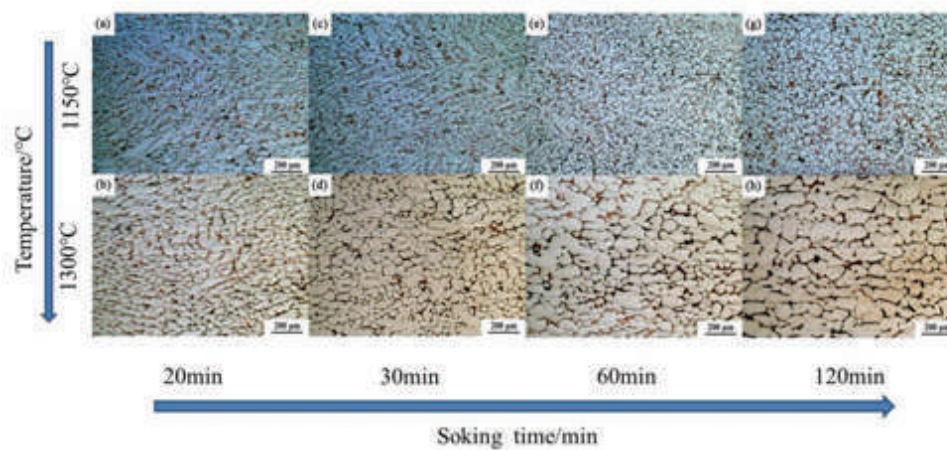


Figure 7. Metallographic photograph: (a) 1150 °C, 20min;(b) 1300 °C, 20min;(c) 1150 °C, 30min;(d) 1300 °C, 30min;(e) 1150 °C, 60min;(f) 1300 °C, 60min;(g) 1150 °C, 120min;(h) 1300 °C, 120min.

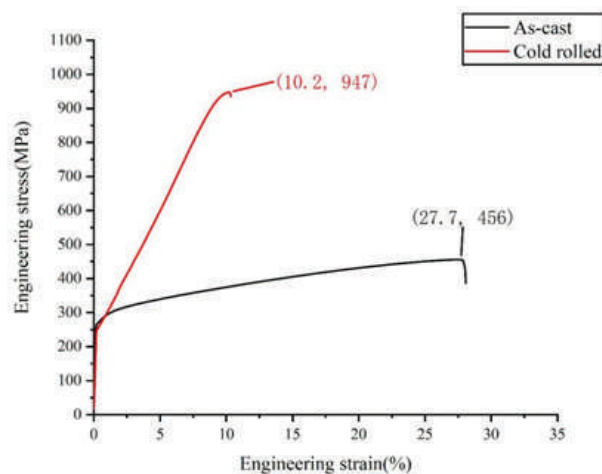


Figure 8. Stress-strain curves of as-cast and rolled alloys.

Figure 9 and Figure 10 show the stress-strain curves of four groups of tensile experiments treated at 1150 °C and 1300 °C for 20min, 30min, 60min and 120min, respectively. As can be seen from Figure 9, the tensile strength of the alloy was 350MPa when the alloy was isothermally treated at 1150 °C for 20min, and the tensile strength increased to 365MPa when the alloy was kept heat preservation for 30min. However, the tensile strength decreased to 335MPa and 305MPa after the isothermal treatment for 60min and 120min. In FIG.10, the tensile mechanical properties of the alloy treated at 1300 °C have the same tend as those of the alloy treated at 1150 °C. The tensile strength was 330MPa at 20min of heat preservation, and slightly increased to 335MPa after 30min of heat preservation.

This shows that the mechanical properties of CoCrCuFeNi high entropy alloy will change with the holding time when the temperature of semi-solid isothermal treatment remains unchanged. When the semi-solid isothermal treatment time is less than 30 min, the mechanical properties of CoCrCuFeNi high entropy alloy become better with the increase of semi-solid isothermal treatment time. When the semi-solid isothermal treatment time is more than 30 min, the mechanical properties of CoCrCuFeNi high entropy alloy become worse with the increase of semi-solid isothermal treatment time.

When the time of semi-solid isothermal treatment is constant, it can be seen that the tensile strength of the alloy at 1300 °C is lower than that at 1150 °C from Figure 9 and 10. The results show that the optimal properties of CoCrCuFeNi high entropy alloy appear in the semi-solid isothermal treatment at 1150 °C for 30min, which is the same as the conclusion obtained in the previous metallographic structure analysis. It may be due to the high degree of grain refinement and microstructure homogenization after treatment at 1150 °C for 30min, so the strength of CoCrCuFeNi alloy is better at this time. After the heat preservation, the copper rich FCC1 phase cannot be supplemented by the liquid phase, resulting in shrinkage or porosity.

On the one hand, the composition has changed because of the exchange of elements in the two phases during the semi-solid isothermal heat treatment. According to the similar study in L.J. Zhang^[17], the content of Cu in low melting point FCC1 phase increased to about 83% and the content of CoCrFeNi decreased after semi-solid treatment. The enrichment of copper in FCC1 phase results in dendrite segregation, and the difference of composition and structure between the two phases becomes larger. The formation of positive mixing enthalpy between Cu and other four components, which indicated that it can repel the other four elements and reduce the affinity of two-phase structure, so the overall plasticity of the sample is reduced^[18]; on the other hand, the solid phase of FCC2 grows up slowly and contacts with each other, the liquid phase of FCC1 is enclosed by the solid phase of FCC2 into a closed region. At the end of heat preservation, the copper rich FCC1 phase will produce shrinkage cavity and porosity due to the lack of liquid supplement during the

water-cooling solidification process. Under the action of semi-solid isothermal treatment, the shrinkage cavity and porosity changes into crack shown in Figure 11, and the higher the holding temperature is, the more obvious the crack is, resulting in an obvious drop of plasticity.

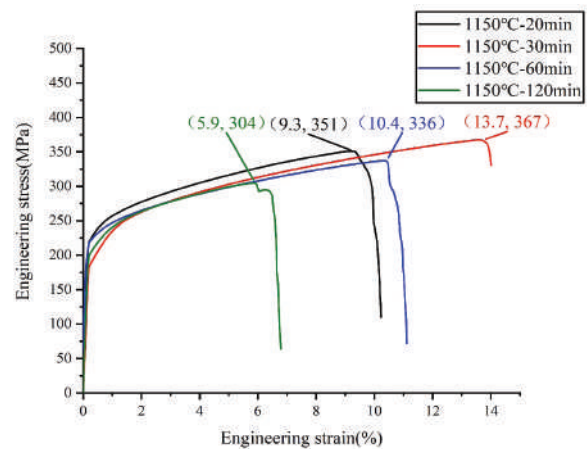


Figure 9. Tensile stress-strain curves of four groups at 1150 °C.

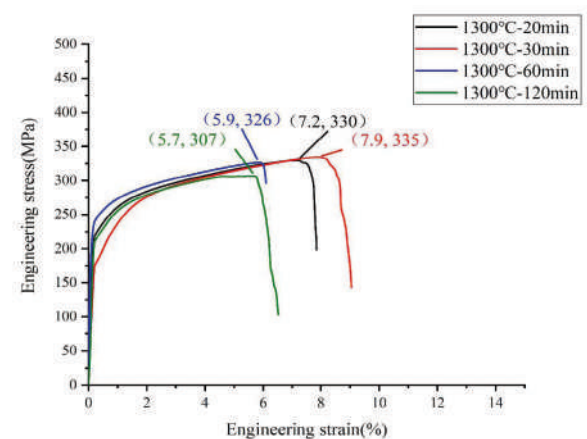


Figure 10. Tensile stress-strain curves of four groups at 1300 °C.

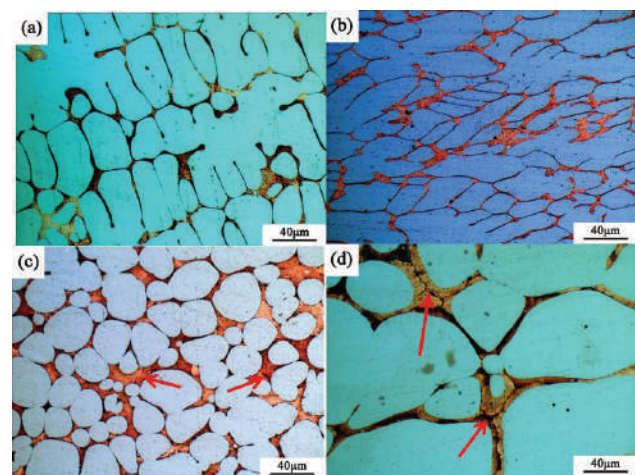


Figure 11. (a) high power in casting state (b) high power in rolling state (c) high power in 1150 °C for 120min (d) high power in 1300 °C for 120min.

Conclusions

1) The as-cast CoCrCuFeNi high-entropy alloy has two simple FCC phases, which exists in the form of intercrossing between dendrites and dendrites. The phase structure is not changed by rolling and semi-solid isothermal treatment. The as-cast alloy has 28% excellent plasticity.

2) After cold rolling with 63% deformation, the strength of CoCrCuFeNi high entropy alloy increased about 107%. Cold rolling pre deformation destroys the continuous distribution of dendrites, and the deformation energy accumulates at the grain boundary. In the stage of remelting and heat preservation, the release of stored internal energy can promote the melting of grain boundary, increase the proportion of liquid phase and improve the dendrite fuse.

3) The orthogonal experiment of semi-solid isothermal treatment was carried out on the rolled CoCrCuFeNi high entropy alloy. The results show that for the same holding time, with the increase of holding temperature, the microstructure grains become larger and the mechanical properties decrease; with the same holding temperature, the holding time of the optimal tensile properties is 30min, and the optimal semi-solid isothermal treatment parameters are 1150°C, 30min. The corresponding optimum elongation plastic variable is 13.7%, and the strength is 365MPa.

4) The tensile strength and plasticity of the high entropy alloy after isothermal treatment in solid state are lower than that in as-cast. The reason is that the micro cracks in rolling and the oxidation of the cracks in the process of isothermal treatment form, which results in the mechanical properties of the alloy after isothermal treatment is inferior to that of the as cast alloy. More experiments are needed to find other ways to strengthen the high entropy alloy.

Author Contributions: The experiment, data analysis and writing of this article are completed by Lajie Wang. X J Yang puts forward the idea of this article. Jiao Xiong and Jun Liu assist Wang in completing the experiment and writing.

Acknowledgments: This work was supported by the National Natural Science Foundation of China (Nos. 13006707), Science and Technology Project of the Education Department of Jiangxi Province (Nos.171468,181481)

References

- [1] J.W. Yeh, S.K. Chen, S.J. Lin, et al. Nanostructured high-entropy alloys with multiple principal elements: novel alloy design concepts and outcomes. [J]. *Adv. Eng. Mater* 2004 6. 299-303.
- [2] Y. Zhang, T.T. Zuo, Z. Tang, et al *Microstructures and properties of high-entropy alloys*[J]. *Prog. Mater. Sci* 2014 61, 1-93.
- [3] Huang Yuansheng, Cai minghong, Ye Junwei. Study on optical properties of AlCoCrCu_{0.5}NiFe high entropy alloy

- oxide thin film [J]. *Surface technology* 2016(2), 129-133.
- [4] Chen Yongxing, Zhu Sheng, Wang Xiaoming, et al. Laser cladding Al_{0.4}CoCu_{0.6}NiSi_{0.2}Ti_{0.25} layer of abrasion resistance and high entropy alloys forming mechanism analysis [J]. *Journal of Hot Working Process* 2018,47,1-6.
- [5] Jingwen Qiu, Zhengfan Fu, Di Pan, et al. The Wear Behavior of High-Entropy Alloy Particles Reinforced Titanium Alloy Composite[J]. *Journal of Materials Science* 2018, 8(10), 1007-1015.
- [6]. Z.Q. Fu, W.P. Chen, H.M. Wen, et al. Microstructure and strengthening mechanisms in an FCC structured single-phase nanocrystalline Co₂₅Ni₂₅Fe₂₅Al_{7.5}Cu_{17.5} high-entropy alloy.[J]. *Acta Mater* 2016 107, 59-71.
- [7] B. Schuh, F. Mendez-Martin, B. Volker, et al. Mechanical properties, microstructure and thermal stability of a nanocrystalline CoCrFeMnNi high-entropy alloy after severe plastic deformation[J]. *Acta Mater* 2015 96, 258-268.
- [8] H. Shahmir, T. Mousavi, J. He, Z. Lu, et al. Microstructure and properties of a CoCrFeNiMn high-entropy alloy processed by equal-channel angular pressing[J]. *Mater. Sci. Eng. A* 2017, 705, 411-419.
- [9] M.C. Flemings. Behavior of metal alloys in the semisolid state *Metall. Trans. A* 1991, 22,269-293.
- [10] T.J. Chen, R.Q. Wang, Y. Ma, et al. Effects of processing parameters on microstructure and ultimate tensile strength of thixoformed AM60B magnesium alloy.[J]. *Mater. Res* 2012, 15, 687-697.
- [11] H.V. Atkinson. Modelling the semisolid processing of metallic alloys[J]. *Prog. Mater. Sci* 2005, 50, 341-412.
- [12] J. Jiang, Y. Wang, G. Xiao, et al. Comparison of microstructural evolution of 7075 aluminum alloy fabricated by SIMA and RAP[J]. *J. Mater. Process. Technol* 2016, 238, 361-372.
- [13] Q. Chen, S.J. Luo, Z. Zhao. Microstructural evolution of previously deformed AZ91D magnesium alloy during partial remelting[J]. *J Alloys Compd* 2009, 477, 726-731
- [14] L Rogal. Semi-solid processing of the CoCrCuFeNi high entropy alloy[J]. *Mater. Des* 2017, 119, 406-416.
- [15] A. Takeuchi, A. Inoue. Classification of bulk metallic glasses by atomic size difference, heat of mixing and period of constituent elements and its application to characterization of the main alloying element[J]. *Mater. Trans* 2006,46, 2817-2829.
- [16] H.V. Atkinson, K. Burke, G. Vaneetveld. Recrystallisation in the semi-solid state in 7075 aluminium alloy[J]. *Mater. Sci. Eng. A* 2008, 490, 266-276.
- [17] Zhang L J , Fan J T , Liu D J , et al. The microstructural evolution and hardness of the equiatomic CoCrCuFeNi high-entropy alloy in the semi-solid state[J]. *Journal of Alloys and Compounds*, 2018, 745,75-83.
- [18] R.N. Singh, F. Sommer Segregation and immiscibility in liquid binary alloys Rep. Prog. Phys. 1997,60,57-150.

Application of Millimeter 3D Automatic Paving System in Highway Engineering Construction

Yi DONG^{1*}, Jie WANG², Yijia MAO³, Hua LI⁴

1 ChangZhou Communications Construction Administration Co.Ltd , ChangZhou, China

2 Jiangsu Easttrans Intelligent Control Technology Group Co.Ltd , NanJing, China

3 Jiangsu Easttrans Intelligent Control Technology Group Co.Ltd , NanJing, China

4 Jiangsu Easttrans Intelligent Control Technology Group Co.Ltd , NanJing, China

*Corresponding Author: Yi DONG, Zidong 2#, Maqun Street, Nanjing 210000, P.R. China, 419220471@qq.com

Abstract:

In the construction of asphalt mixture pavement, there are many paving construction procedures, high requirements for machinery and personnel, unreasonable technology and so on. In this paper, the millimeter-scale 3D automatic paving control technology of asphalt mixture pavement is studied with an engineering example. From the analysis of the test results in the later stage of construction, it can be seen that the technology has achieved the goal of high precision paving, and the successful application of the technology provides valuable reference experience for similar asphalt concrete pavement construction in the future.

Keywords: Asphalt pavement; Millimeter grade; 3D paving control technology; Engineering application

1. Introduction

Due to its advantages of safe and comfortable driving, no dust on sunny days, no mud on rainy days and strong self-repairing, asphalt concrete surface layer is widely used in the construction of high-grade highway in China, especially in the Eastern and Western regions, where the temperature difference between winter and summer is large^[1]. However, at present, the early damage of asphalt concrete pavement is quite serious, and the fine construction of asphalt concrete pavement construction is particularly important, especially the paving link of asphalt concrete. Traditional pavement paving construction process is more, the requirements of machinery and personnel coordination, weather and other aspects are relatively high. In the design of turning, super elevation curve and other cross-slope changes, it is almost impossible to accurately set the hanging line^[2]. With the rapid development of science and technology, the concept of pavement 3D paving has gradually emerged. Through the application of advanced information technology such as high-precision positioning, intelligent sensors, three-dimensional modeling, data analysis and so on, the traditional roadbed construction machinery has eyes, has a sense, makes it can be accurately realized to control the smoothness in pavement construction and, greatly

simplifies the construction procedure. Especially, it reduces the measuring frequency, improves the benefit and controls the quality^[3-4]. Lu^[5] described the main equipment and technological process of 3D paving system, and analyzed the effect of 3D automatic paving technology applied to pavement construction based on the reconstruction and expansion project of liuzhou to nanning expressway. Liu^[6] introduced the construction process of 3D automatic paver control system, and compared the traditional construction technology, analyzed the advantages of 3D automatic paver system construction, providing valuable experience for the development of 3D paver technology.

2. Principle of 3D paving technology

2.1. Technical principle

Paver is the main machine used for laying structural layer and surface layer. During the construction of the automatic control system of 3D paver, the total station installed at the control point transmits the captured coordinates to the control box of the paver control system through the data radio in real time. After comparing the display control box with the design data, the elevation correction information is transmitted to the control box. At this time, the control box sends out instructions, and the hydraulic cylinder is driven

3. Field implementation plan

3.1. Test scheme

In order to compare the difference between 3D paving construction and traditional paving construction, the experiment is carried out in parallel with two methods. The specific requirements are as follows.

(1) system configuration

Paver 1 is equipped with 3-D paving control system and Paver 2 adopts the traditional paving control system.

(2) Programme description:

Paver1 is equipped with 3D paving control system. Paver2 adopts the traditional 2D paving control mode. Figure 1 is the schematic test plan. The right side of paver1 is equipped with a target, which is guided and controlled by the intelligent robot of total station; the left side is controlled by the cross slope sensor. There is no need to lay piles and hang wires or aluminium beams on both sides. The left side of paver2 uses the traditional 2D mode to refer to the paver1's paved surface to ensure the perfect joints; the right side still needs lay piles and hang wires / aluminium beam manually, and uses the traditional 2D control mode to pave.



Figure 2. Schematic diagram of paving scheme

3.2. The Collection Scheme of Test Data

In order to compare the difference of personnel, efficiency and quality between traditional paving and 3D paving construction technology. According to each kilometer as a unit, the data acquisition section of 3D paving and the traditional construction section are one kilometer each, corresponding stake numbers are K31+000-K32+000 and K32+000-K33+00 in the northern half. The data acquisition requirements are as follows.

3.2.1 Personnel data

According to the statistics of manual consumption in this test section, the time consumption of labor workers (auxiliary workers), mechanical operators (drivers of pavers), surveyors (engineers and technicians), and testers was collected under the two conditions of 3D paving construction and traditional construction.

3.2.2 Line detection

After the field rolling, the gradient of the center of the paving area is measured by total station in the 3D paving area and the traditional paving area. The data acquisition density is 100 meters.

3.2.3 Data Acquisition of Quality Inspection

(1) thickness

Total Station Measuring Method: Total Station is used to measure the elevation difference of the same point before and after paving construction. Six points are collected for each section of 10 meters, three points for the construction section of the left paver and three points for the construction section of the right paver. Thickness nephogram of 3D paving area and traditional paving area

is generated.

Core drilling sampling method: Within the range of K32+000-K33+00, 6 points are collected for each section of 200 meters using core drilling machine, which are 3 points for the construction section of the left paver and 3 points for the construction section of the right paver. Within K31+000-K32+000, in the construction area of the left paver, there is a section every 200 meters and three points for each section.

(2) Compaction degree

Marking the core samples obtained from the drill core, and measuring the compactness of each core sample by Marshall method.

(3) Planeness

Measuring the pavement smoothness of 3D paving section and traditional construction section by eight-wheel instrument.

4. Analysis of experimental data

4.1. Personnel data

According to the statistics of construction site, there are seven types of work involved in asphalt pavement construction, namely: paver mechanical driver, surface treatment worker, joint treatment worker, road surface treatment worker, measurement control worker, quality inspector, management personnel. From Table 2, it can be seen that the number of workers required by each paver is 12 by using 3D paving construction technology, and 20 by using traditional paving construction technology. Therefore, the use of 3D paving technology can save 40%

of human resources.

4.2 Line detection

The longitudinal gradient of the center line of the left paving area of K31+000-K32+000 and K32+000-K33+00 is obtained by total station. The traditional paving area K31+000-K32+000 obtains 10 data of a vertical slope every 100m, while the 3D paving area K32+000-K33+000 obtains

10 data of a vertical slope every 100m. The specific data are shown in Table 3. It can be seen from the table that the variation coefficient CV of longitudinal slope is -0.54 and that of traditional paving construction technology is -1.43. It shows that the 3D paving construction technology can better control the line type and the slope control is more accurate.

Table 2. Statistics of labor consumption

number	Personnel situation	3D paving / number of people	Traditional paving / number of people
1	paver mechanical driver	3	3
2	surface treatment worker	2	3
3	joint treatment worker	1	3
4	road surface treatment worker	1	3
5	measurement control worker	2	4
6	quality inspector,	1	1
7	management personnel	2	3
	total	12	20

Table 3. data of line detection

number	traditional paving construction		3D paving construction	
	stake number	Longitudinal gradient (%)	stake number	Longitudinal gradient (%)
1	K31+000	0.02%	K32+000	-0.14%
2	K31+100	-0.10%	K32+100	-0.14%
3	K31+200	-0.01%	K32+200	-0.14%
4	K31+300	-0.01%	K32+300	-0.14%
5	K31+400	-0.04%	K32+400	-0.12%
6	K31+500	-0.04%	K32+500	-0.12%
7	K31+600	0.01%	K32+600	-0.05%
8	K31+700	-0.21%	K32+700	-0.04%
9	K31+800	-0.03%	K32+800	-0.07%
10	K31+900	-0.03%	K32+900	-0.07%
		0.00%		-0.09%
11	K32+000	-0.02%	K33+000	-0.06%
		-0.15%		-0.01%
statistical analysis	standard deviation SD	0.08%	standard deviation SD	0.05%
	average value	-0.05%	average value	-0.09%
	Coefficient of variation CV	-1.43	Coefficient of variation CV	-0.54

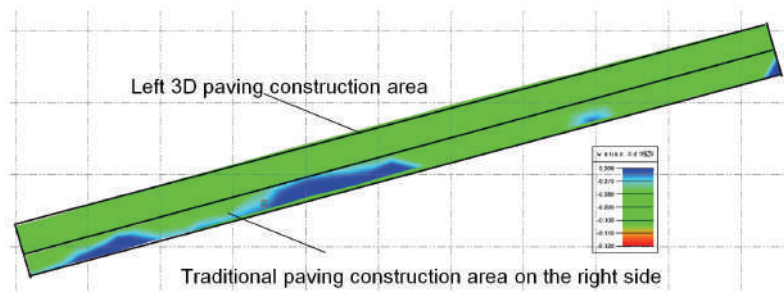
4.3 Data Acquisition of Quality Inspection

4.3.1 thickness

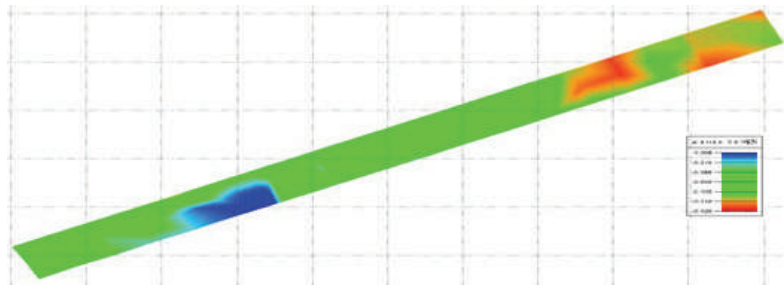
(1) Method of total station measurement

Figure 2 shows the thickness of asphalt pavement obtained by total station. From the figure, it can be seen

that the thickness of 3D paving construction area is uniform and the error is controlled within 1 cm. In the traditional construction area, the paving is too thick or thin in some areas. The blue area in the figure is over 1 cm thick, and the red area is over 1 cm thin.



Nephogram of 3D paving thickness (K32+000-k33+000)



Nephogram of traditional paving thickness (K31+000-k32+000)

Figure 3. Thickness nephogram

(2) Method of core sampling

According to the core sampling detection scheme, drilling cores were sampled in the field, and the height of each core sample was measured by vernier caliper. The average thickness of each core sample was taken as the layer thickness of the sampling point. A total of 30 sets of data were obtained. The specific data are shown in Table 4. It can be seen from the table that the average thickness of 3D paving construction technology and traditional paving construction technology are 79.3 mm and 83.3 mm, respectively, which meet the requirements of the specifications, but the traditional paving thickness is too large, resulting in waste of asphalt mixture and increasing construction costs. From the aspect of thickness uniformity, the standard deviation of thickness between 3D paving construction technology and traditional paving construction technology is 1.0 and 6.5, respectively, which indicates that the performance of thickness control of 3D

paving construction technology is much higher than that of traditional paving technology.

4.3.2 Compaction degree

By using Marshall method, the core samples obtained from field drilling are tested for compactness. A total of 30 sets of data are obtained. The specific data are shown in Table 5. It can be seen from the table that the representative values of compactness of 3D paving construction technology and traditional paving construction technology are more than 98, and the compaction quality is qualified. However, the standard deviation of compactness in 3D paving construction area is 0.9, which is much smaller than the standard deviation of compactness in traditional paving construction area of 2.6. This is due to 3D paving technology, the control thickness is more uniform, and the compaction quality is more uniform under the same rolling conditions.

Table 4. Data of Core Sampling Thickness Detection

3D Paving Construction			Traditional paving construction		
Location of measuring points		thickness (mm)	Location of measuring points		thickness (mm)
stake number	Horizontal distance (m)		stake number	Horizontal distance (m)	
K32+900	2	78.5	K31+900	2	81.5
	4	78.6		4	85.2
	6	79.6		6	86.9
K32+700	2	80.1	K31+700	2	91.6
	4	79.3		4	90.3
	6	78.9		6	95.7

3D Paving Construction			Traditional paving construction		
Location of measuring points		thickness (mm)	Location of measuring points		thickness (mm)
stake number	Horizontal distance (m)		stake number	Horizontal distance (m)	
K32+500	2	78.6	K31+500	2	73.5
	4	79.3		4	84.4
	6	80.4		6	78.4
K32+300	2	79.9	K31+300	2	76.6
	4	80.4		4	75.9
	6	79.3		6	88.6
K32+100	2	80.2	K31+100	2	82
	4	79.9		4	82.9
	6	76.5		6	75.8
data type		Number of measurements (points)	Prescribed value (mm)	average value (mm)	standard deviation
3D Paving Construction		15	80	79.3	1.0
Traditional paving construction		15	80	83.3	6.5

Table 5. Data for compactness testing

3D Paving Construction			Traditional paving construction		
Location of measuring points		Compaction degree (%)	Location of measuring points		Compaction degree(%)
stake number	Horizontal distance(m)		stake number	Horizontal distance(m)	
K32+900	2	98.5	K31+900	2	98.0
	4	100.6		4	101.1
	6	98.5		6	101.5
K32+700	2	100.7	K31+700	2	100.2
	4	98.9		4	99.1
	6	99.5		6	98.9
K32+500	2	98.1	K31+500	2	97.6
	4	99.9		4	98.7
	6	100.9		6	99.2
K32+300	2	98.8	K31+300	2	100.2
	4	100.0		4	98.3
	6	100.4		6	99.9
K32+100	2	100.0	K31+100	2	99.6
	4	98.5		4	101.0
	6	100.4		6	108.6
data type	Number of measurements (points)	Prescribed value (%)	average value (%)	standard deviation	Representative value (%)
3D Paving Construction	15	98	99.6	0.9	99.1
Traditional paving construction	15	98	100.1	2.6	98.9

4.3.3 Planeness

After the construction of asphalt pavement completed, the effects of 3D paving and traditional paving are tested by eight-wheel planeness meter. The results are shown in Table 6.

Table 6 shows that the planeness of asphalt pavement is less than the allowable value (1.2 mm) and the qualified

rate is 100% using 3D paving technology. The planeness of asphalt pavement construction fluctuates greatly using traditional paving technology, the maximum value is 1.79 mm, which is larger than the allowable value, and the qualified rate is only 61%. This indicates that the 3D paving technology can improve the planeness of asphalt pavement.

Table 6. Testing data of compactness

Technology	stake number	Number of tests	Allowable value (mm)	average value (mm)	Maximum value mm)	minimum value (mm)	Pass rate (%)
3D paving construction	K32+000-K33+00	24	1.2	0.58	0.71	0.33	100
Traditional paving construction	K31+000-K32+000	24	1.2	1.4	1.79	0.89	70

5 Conclusion

3D paving technology does not need to lay piles and erect aluminium beams to greatly reduce construction survey work. Site can be put into work quickly. Digital construction can reduce about 40% of surveying and assistant personnel, make construction site more concise and efficient, reduce potential safety hazards, realize millimeter accuracy level control and improve paving accuracy by about 30%, the intelligent paver does not need the operator to control the ironing elevation and cross slope. Compared with the traditional construction, the work efficiency can be increased by about 50%. It reduces the dependence on the roughness of the base and ensures the accuracy of the pavement in the error range to the greatest extent.

References

- [1] Wang Jiahui. Early Problems of Asphalt Concrete Pavement and Preventive Measures [J]. Highway Engineering, 2012(17):63-65.
- [2] Guo Xiaohong, Du Zhengde, Guo Jiaying. Theory and

Practice in the Mechanical Construction System of the Asphalt Paving (VII)—The Computer Simulation of Mechanical Construction System[J]. JOURNAL OF CHONGQING JIAOTONG INSTITUTE, 1996.

- [3] Lei Xiaolei, Li Gang. 3 Applied Research of 3D Paving Control Technology in Asphalt Pavement Works [J]. Road & Traffic Engineering, 2018(5):20-24..
- [4] Zu Mingxing. Research on 3D Intelligent Paving Application of Asphalt Concrete Pavement [J]. Road Engineering, 2018, 136(11):17-20.
- [5] Lu Qiaoyu. Application Analysis of 3DTechnology Pavement Construction in Highway Engineering[J]. Western China Communications Science & Technology, 2018.
- [6] Liu Fuxu. Discussion on the Application of 3D Automated Paving System in Highway Engineering Construction[J]. Western China Communications Science & Technology, 2018.

Publisher: Viser Technology Pte. Ltd.

URL: www.viserdata.com

Add.:21 Woodlands Close, #08-18,

Primz Bizhub SINGAPORE (737854)